

The Efficacy of Semantics-Preserving Transformations in Self-Supervised Learning for Medical Ultrasound

Blake VanBerlo, Alexander Wong, Jesse Hoey, and Robert Arntfield

Abstract—Data augmentation is a central component of joint embedding self-supervised learning (SSL). Approaches that work for natural images may not always be effective in medical imaging tasks. This study systematically investigated the impact of data augmentation and preprocessing strategies in SSL for lung ultrasound. Three data augmentation pipelines were assessed: (1) a baseline pipeline commonly used across imaging domains, (2) a novel semantic-preserving pipeline designed for ultrasound, and (3) a distilled set of the most effective transformations from both pipelines. Pretrained models were evaluated on multiple classification tasks: B-line detection, pleural effusion detection, and COVID-19 classification. Experiments revealed that semantics-preserving data augmentation resulted in the greatest performance for COVID-19 classification – a diagnostic task requiring global image context. Cropping-based methods yielded the greatest performance on the B-line and pleural effusion object classification tasks, which require strong local pattern recognition. Lastly, semantics-preserving ultrasound image preprocessing resulted in increased downstream performance for multiple tasks. Guidance regarding data augmentation and preprocessing strategies was synthesized for practitioners working with SSL in ultrasound.

Index Terms—Data augmentation, Machine learning, Self-supervised learning, Ultrasound

I. INTRODUCTION

AUTOMATED interpretation of medical ultrasound (US) images is increasingly implemented using deep learning [1]. Deep neural networks (DNN) achieve strong performance for applications in US imaging, such as distinguishing benign from malignant liver lesions [2], estimating left ventricular end-diastolic and end-systolic volumes [3], and screening for pneumothorax [4].

Despite early successes, investigators are limited by the lack of publicly available datasets [5], [6]. When available, researchers use private collections of US examinations, as they may contain far more samples. Given the expense of manual annotation, many are turning to self-supervised learning (SSL) methods to pretrain DNNs using large, unlabeled collections

This work has been submitted to Medical Image Analysis for possible publication. Copyright may be transferred without notice, after which this version may no longer be accessible. This study was funded by the Natural Sciences and Engineering Research Council of Canada, as B. VanBerlo is a Vanier Scholar (FRN 186945). Computational resource support was also provided by Compute Ontario (computeontario.ca) and the Digital Research Alliance of Canada (alliance.can.ca).

B. VanBerlo is with the Cheriton School of Computer Science at the University of Waterloo, ON N2L 3G1 Canada (e-mail: bvanberl@uwaterloo.ca).

A. Wong is with the Department of Systems Design Engineering at the University of Waterloo, ON N2L 3G1 Canada.

J. Hoey is with the Cheriton School of Computer Science at the University of Waterloo, ON N2L 3G1 Canada.

R. Arntfield is with the Schulich School of Medicine and Dentistry at Western University, ON N6A 3K7 Canada.

of US data [7]. These SSL-pretrained backbone DNNs may be fine-tuned for supervised learning tasks of interest.

An important category of SSL methods for computer vision is the *joint embedding architecture*, which is characterized by training DNNs to produce similar vector representations for pairs of related images. The most common method for retrieving related pairs of images from unlabeled datasets is to apply random transformations (i.e., data augmentation) to an image, producing two distorted views. The choice of random transformations steers the invariance relationships learned by the backbone.

In this study, we proposed and assessed data preprocessing and data augmentation strategies designed to preserve semantic content in medical ultrasound images (Fig 1). We compared handcrafted domain-specific augmentation methods against standard SSL data augmentation practices. We found that US-specific transformations resulted in the greatest improvement in performance for COVID-19 classification – a diagnostic task – on a public dataset. Experiments also revealed that standard cropping-based augmentation strategies outperformed US-specific transformations for object classification tasks in lung US. Lastly, ultrasound-specific semantics-preserving preprocessing was found to be instrumental to the success of pretrained backbones. In summary, our contributions are as follows:

- Semantics-preserving image preprocessing for SSL in US
- Semantics-preserving data augmentation methods designed for US images
- Comparison of multiple data augmentation strategies for SSL for multiple types of lung US tasks
- Recommendations for practitioners working with unlabeled US datasets

To our knowledge, this study is the first to quantify the impact of data augmentation methods for SSL with US. We are hopeful that the results and lessons from this study may contribute to the development of foundation models for medical US.

II. BACKGROUND

A. Data Augmentation in Self-Supervised Learning

The joint embedding class of SSL methods is characterized by the minimization of an objective function that, broadly speaking, encourages similarity of related pairs of inputs. Semantically related pairs of images (i.e., *positive pairs*) are sampled from unlabeled datasets according to a *pairwise relationship*. If the SSL pairwise relationship is satisfied for samples exhibiting the same class, SSL methods will likely

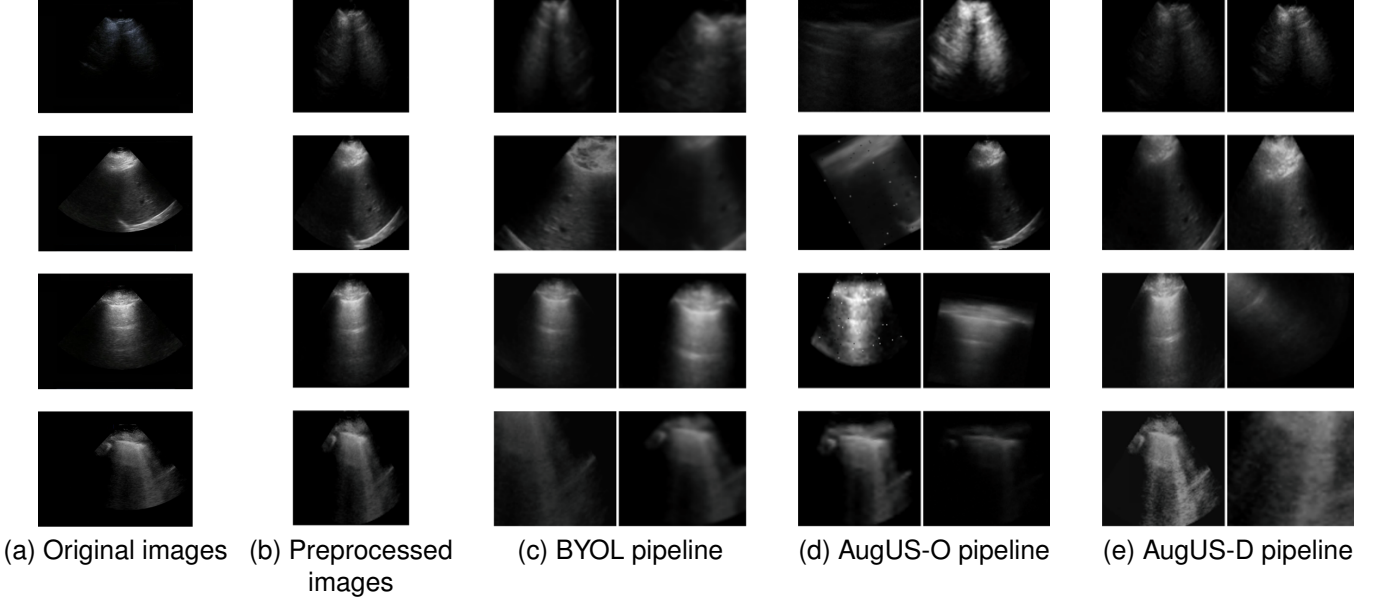


Fig. 1. Examples of the preprocessing and data augmentation methods in this study. (a) Original images are from ultrasound exams. (b) Semantics-preserving preprocessing is applied to crop out areas external to the field of view. (c) The BYOL pipeline is a commonly employed data augmentation pipeline in self-supervised learning. (d) The AugUS-O pipeline was designed to preserve semantic content in ultrasound images. (e) AugUS-D is a hybrid pipeline whose construction was informed by empirical investigations into the BYOL and AugUS-O pipelines.

improve the performance of a classifier [8]. Most joint embedding methods rely on data augmentation to define the pairwise relationship. Some studies have used meta-data or known relationships between samples to identify related pairs [9]–[11]; however, the availability of such information is rare. The choice of data augmentation transformations is therefore crucial, as it dictates the invariances learned [12]. However, the set of useful invariances differs by the image modality and downstream problem(s) of interest. Despite this, studies continue to espouse the data augmentation pipeline used in the Bring Your Own Latent (BYOL) method, which includes random crops, horizontal reflection, color jitter, Gaussian blur, and solarization [13]. Random rotation is an example of a transformation not found in the BYOL pipeline that represents an important invariance relationship for many tasks in medical imaging. For example, random rotation has been applied in SSL pretraining with magnetic resonance exams of the prostate [14]. Moreover, the authors did not use BYOL’s Gaussian blur transformation because it may have rendered the images uninterpretable.

B. Joint Embedding Self-Supervision in Ultrasound

Recent studies have examined the use of joint embedding SSL methods for US interpretation tasks, such as echocardiogram view classification [15], left ventricle segmentation [16], and breast tumor classification [17]. Some have proposed positive pair sampling schemes customized for US. The USCL method and its successors explored contrastive learning methods where the positive pairs were weighted sums of images from the same US video [18]–[20]. Other methods have studied the use of images from the same video as positive pairs [11], [21]. In these studies, the set of transformations

TABLE I
BREAKDOWN OF THE UNLABELED, TRAINING, VALIDATION, AND TEST SETS IN THE PRIVATE DATASET. x/y INDICATES THE NUMBER OF LABELED VIDEOS IN THE NEGATIVE AND POSITIVE CLASS FOR EACH BINARY CLASSIFICATION TASK.

	Local				External
	Unlabeled	Train	Validation	Test	Test
Patients	5571	1702	364	364	168
Videos	59309	5679	1184	1249	925
AB labels	N/A	2067/999	459/178	458/221	286/327
PE labels	N/A	789/762	176/142	162/158	68/110
PL labels	N/A	200	39	45	0

were a subset of the BYOL data augmentation pipeline, occasionally with different hyperparameters. Few studies have proposed US-specific data augmentation methods for SSL. A recent study by Chen *et al.* [22] applied BYOL and SimCLR to pretrain 3D convolutional DNNs with specialized data augmentation for lung consolidation detection in US videos, observing that temporal transformations were contributory to their problem. This study builds on previous literature by proposing and comparing domain-specific data augmentation and preprocessing method for multiple types of downstream tasks.

III. MATERIALS & METHODS

A. Datasets and Tasks

We assessed the methods in this publication using a combination of public and private data. COVIDx-US is a public COVID-19 lung US dataset consisting of 242 publicly sourced videos, acquired from a variety of manufacturers and sites [23]. Each example is annotated with one of the following classes:

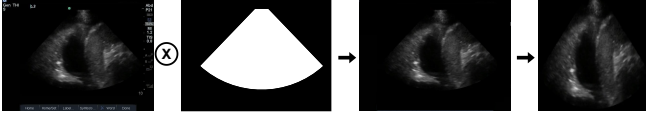


Fig. 2. Raw ultrasound images are preprocessed by applying a mask that preserves only the field of view, then cropped according to the bounds of the field of view.

normal, COVID-19 pneumonia, non-COVID-19 pneumonia, and other lung pathology. Referred to as COVID hereafter, the task is a four-class image classification problem. Since there is no standard test partition, we split the data by patient identifier into training (70%), validation (15%), and test (15%) splits.

The second data source is a private collection of lung ultrasound examinations, and we refer to it as *LUSData*. Access to this data was granted by Western University research ethics board (REB 116838) on January 28, 2021. LUSData contains videos from of parenchymal and pleural views of the lung. A subset of the parenchymal views have labels for the presence of A-lines or B-lines (i.e., the AB classification task). A-lines are reverberation artifacts that indicate normal lung tissue, while B-lines are axial artifacts that indicate fluid or thickness in the lung. A subset of the pleural views are labeled for the presence or absence of pleural effusion (i.e., the PE classification task), which is an accumulation of fluid around the lungs. A small fraction of the parenchymal views in LUSData possess bounding box labels for the pleural line artifact (i.e., the PL object detection task). Most exams in LUSData originated from a local healthcare centre, but a subset were acquired at another centre, which we adopt as an external test set. The labeled examples in the local dataset was split into training (70%), validation (15%), and test (15%) splits by patient. Table I provides the video and class counts of LUSData. Further dataset details are in Appendix A. All models in this study are trained on images, instead of on videos. Classification labels apply to every image in the video. However, individual images within each video labeled for the PL task have bounding box annotations.

B. Semantics-Preserving Preprocessing

The field of view (FOV) in US images is typically surrounded by burnt-in scan parameters, logos, and other details. We estimated the shape of the FOV and masked out all extraneous graphical entities using ultrasound cleaning software (UltraMask, Deep Breathe Inc., London, ON, Canada). Semantic information only exists within the FOV of the US, which typically occupies a fraction of the images. Scaling transformations, such as random cropping, could produce views that largely contain background. Accordingly, we cropped the cleaned images to the smallest rectangle that encapsulates the FOV mask to maximize semantic content in US images. Fig. 2 depicts this semantics-preserving preprocessing workflow. The process was applied to all images in LUSData and COVIDx-US.

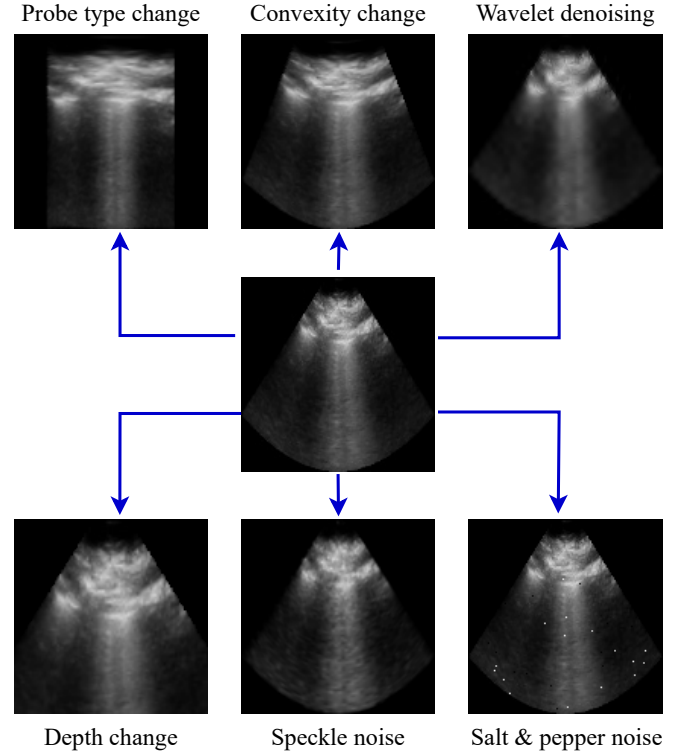


Fig. 3. Examples of ultrasound-specific data augmentation transformations applied to the same US image.

TABLE II
THE SEQUENCE OF TRANSFORMATIONS IN THE BYOL DATA AUGMENTATION PIPELINE [13]

Identifier	Probability	Transformation	Time [ms]
<i>B00</i>	1.0	Crop and resize	0.29
<i>B01</i>	0.5	Horizontal reflection	0.08
<i>B02</i>	0.8	Color jitter.	2.40
<i>B03</i>	0.2	Conversion to grayscale	0.19
<i>B04</i>	0.5	Gaussian blur	0.74
<i>B05</i>	0.1	Solarization	0.15

C. Ultrasound-specific Data Augmentation

Joint embedding SSL is effective when positive pairs contain similar information with respect to downstream tasks [8]. Several SSL studies applied to photographic or medical imaging datasets adopt the BYOL data augmentation pipeline used by Grill *et al.* [13]. The core aim of our study was to determine if semantics-preserving data augmentation would better equip pretrained feature extractors for downstream LUS tasks than the commonly applied BYOL pipeline.

We refer to a *data augmentation pipeline* as an ordered sequence of transformations, each applied with some probability. For clarity, we assign each transformation an alphanumeric identifier and express a data augmentation pipeline as an ordered sequence of identifiers. The BYOL pipeline transformations are detailed in Table II. The table also includes an estimate of the time to transform a single image. Details on how the runtime estimates were calculated are in Appendix A.

We designed the *AugUS-O* pipeline, which was intended to preserve semantic information in the entire US FOV while imposing nontrivial differences across invocations. The transformations in AugUS-O are listed below. Algorithmic details and parameter settings for the BYOL and AugUS-O pipelines are in Appendices A and F, respectively.

- B00: **Probe Type Change:** Inspired by Zeng *et al.*'s work [24], this transformation resamples a US image according to a different field of view (FOV) shape. Linear FOV shapes are converted to curvilinear shapes, while curvilinear and phased array are converted to linear.
- U01: **Convexity Change:** The shape of convex beams can vary, depending on the manufacturer, depth, and field of view of the probe. This transformation modifies the FOV shape such that the distance between x_1 and x_2 is altered, mimicking a change in θ_0 .
- U02: **Wavelet Denoising:** As an alternative to the commonly used Gaussian blur transformation, this transformation denoises an image by thresholding it in wavelet space, according to Birgé and Massart's method [25].
- U03: **Contrast-Limited Adaptive Histogram Equalization:** This transformation enhances contrast by applying locally informed equalization [26].
- U04: **Gamma Correction:** In contrast to standard brightness change transforms, gamma correction applies a nonlinear change in pixel intensity.
- U05: **Brightness and Contrast Change:** The brightness and contrast of the image are modified by applying a linear transform to the pixel values.
- U06: **Depth Change Simulation:** Changing the depth controls on an ultrasound probe impacts how far the range of visibility is from the probe. This transformation simulates a change in depth by applying a random zoom, while preserving the FOV shape.
- U07: **Speckle Noise Simulation:** Speckle noise, Gaussian noise, and salt & pepper (S&P) noise are prevalent in US [27]. This transformation applies Singh *et al.*'s [28] synthetic speckle noise algorithm to the image.
- U08: **Gaussian Noise Simulation:** Multiplicative Gaussian noise is independently applied to each pixel.
- U09: **Salt & Pepper Noise Simulation:** A small, random assortment of pixels are set to black or white.
- U10: **Horizontal Reflection:** The image is reflected about the central vertical.
- U11: **Rotation & Shift:** The image is rotated and translated by a random angle and vector, respectively.

As is common in stochastic data augmentation, each transformation was applied with some probability. Table III gives the entire sequence of transformations, the probability with which each is applied. Visuals of positive pairs produced using the BYOL and AugUS-O augmentation pipelines can be found in Fig. 4a and Fig. 4b, respectively.

We conducted an informal assessment of the similarity of positive pairs. Positive pairs were produced for 50 randomly sampled images, using both the BYOL and the AugUS-O pipelines. The pairs were presented in random order to one of the authors, who is an expert in point-of-care US. They

TABLE III
THE SEQUENCE OF TRANSFORMATIONS IN THE US-SPECIFIC AUGMENTATION PIPELINE

Identifier	Probability	Transformation	Time [ms]
U00	0.3	Probe type change	2.25
U01	0.75	Convexity change	1.92
U02	0.5	Wavelet denoising	5.00
U03	0.2	CLAHE [†]	4.64
U04	0.5	Gamma correction	0.52
U05	0.5	Brightness and contrast change	0.49
U06	0.5	Depth change simulation	1.76
U07	0.333	Speckle noise simulation	3.69
U08	0.333	Gaussian noise	0.28
U09	0.1	Salt & pepper noise	0.18
U10	0.5	Horizontal reflection	0.19
U11	0.5	Rotation & shift	1.42

[†] Contrast-limited adaptive histogram equalization

were aware of the two pipelines, but were not told which pipeline produced each pair. The expert was asked to mark the pairs they believed conveyed the same clinical impression. We observed that 58% of pairs produced with the BYOL pipeline were marked as similar, whereas 70% of the AugUS-O pairs were marked as similar. While not conclusive, this check added credence to the semantics-preserving intention of the design.

D. Discovering Semantically Contributory Transformations

A major aim of this work was to explore the utility of various data augmentation schemes during pretraining. As such, we conducted leave-one-out analysis for each of the BYOL and AugUS pipelines to estimate the impact of each transformation on models' ability to solve downstream classification tasks. We pretrained separate models on the unlabeled portion of LUSData, using an altered version of a pipeline with one transformation omitted. We then conducted 10-fold cross-validation on the LUSData training set for downstream classification tasks for each pretrained model. The median cross-validation test performance for each model pretrained using an ablated pipeline was compared to a baseline model that was pretrained with the entire pipeline. The experiment was conducted for both the BYOL and AugUS pipelines. Any transformations that, when omitted, resulted in worsened performance on either AB or PE were deemed contributory.

E. Training Protocols

We adopted the MobileNetV3Small architecture [29] for all experiments in this study and pretrained using the SimCLR method [30]. MobileNetV3Small was chosen due to its real-time inference capability on mobile devices and its use in prior work by VanBerlo *et al.* for similar tasks [31]. Images were resized to 128×128 pixels prior to the forward pass. Unless otherwise stated, backbones (i.e., feature extractors) were initialized using ImageNet-pretrained weights [32] and were pretrained using the LARS optimizer [33] with a batch size of 512, a base learning rate of 0.2 and a linear warmup with cosine decay schedule. Pretraining was conducted for 3

epochs with 0.3 warmup epochs for LUSData, and 100 epochs with 10 warmup epochs for COVIDx-US.

To conduct supervised evaluation, a perceptron classification head was appended to the final pooling layer of the backbone. Classifiers were trained using stochastic gradient descent with a momentum of 0.9 and a batch size of 512. The learning rates for the backbone and head were 0.002 and 0.02, respectively; each was annealed according to a cosine decay schedule. Training was conducted for 10 epochs on LUSData and 30 epochs on COVIDx-US. Unless otherwise stated, the weights corresponding to the epoch with the lowest validation loss were retained for test set evaluation.

Although this study focused on classification tasks, we also evaluated backbones on the PL object detection task using the Single Shot Detector (SSD) method [34]. SSL-pretrained backbones were used as the convolutional feature extractor. Architectural and training details for SSD are in Appendix R.

Code for the experiments and transformations will be shared in a public GitHub repository upon publication.

IV. RESULTS

A. Transformation Leave-one-out Analysis

A leave-one-out analysis was conducted to discover which transformations in each of the BYOL and AugUS-O pipelines were contributory to downstream task performance. We pre-trained backbones using versions of each pipeline with one transformation omitted. The private LUSData training set was split by patient into 10 disjoint subsets. For each pretrained backbone, 10-fold cross-validation was conducted to obtain estimates of the performance of linear classifiers trained on its output feature vectors. The maximum validation area under the receiver operating curve (AUC) across epochs was recorded. Omitted transformations that resulted in statistically significant lower validation AUC for either the AB or PE task were included in a third pipeline.

We conducted statistical testing to compare each of the BYOL and AugUS-O pipelines, and for each of the AB and PE tasks (described in Section III-A). Friedman's Test for multiple comparisons [35] was conducted, with significance level 0.05. When significant differences were found, we performed the Wilcoxon Sign-Rank Test [36] to compare the test AUCs from each ablated model to the baseline's test AUCs. To control for false positives, the Holm-Bonferroni correction [37] was applied to keep the family-wise significance level at 0.05.

Table IV details the results of the leave-one-out analysis. Friedman's Test detected differences in performance on both the AB and PE tasks when pretrained using the BYOL pipeline, but only the AB task exhibited differences when pretrained with the AugUS-O pipeline. As shown in Table IV, the set of transformations that exhibited statistically significant reductions in test AUC for at least one task when excluded were crop & resize (B00), color jitter (B02), CLAHE (U03), and rotation & shift (U11). Appendix R provides all test statistics from this investigation. The random crop and resize transformation (B00) Of note is the sharp decrease in performance without the random crop and resize (B00), indicating that it is a critical transformation.

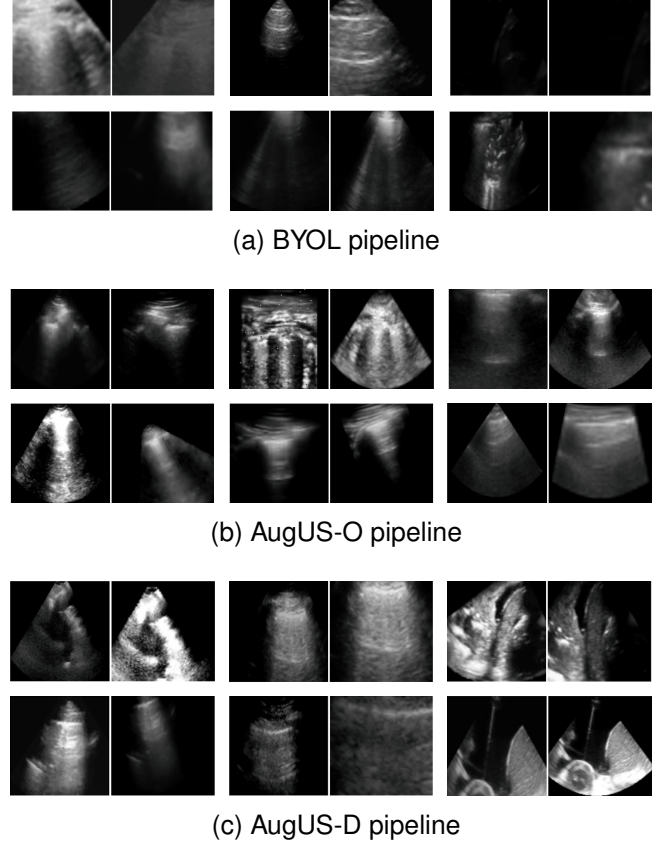


Fig. 4. Examples of positive pairs produced using each of the BYOL, AugUS-O, and AugUS-D data augmentation pipelines.

Using these transformations, we constructed a distilled pipeline that consists only of the above transformations. Referred hereafter to as *AugUS-D*, the pipeline is expressed as the following sequence: *[U03, B02, U11, B00]*. Fig. 4c provides some examples of positive pairs produced with AugUS-D. For more examples of pairs produced by each pipeline, see Appendix R.

B. Object Classification Task Evaluation

The BYOL, AugUS-O, and AugUS-D pipelines were compared in terms of their performance on multiple downstream tasks. Model backbones were pretrained using each of the data augmentation pipelines on the union of the unlabeled and training sets in LUSData. Linear evaluation and finetuning experiments were performed according to the procedure explained in Section III-E. In this section, we present results on the two object classification tasks: A-line vs B-line classification (AB) and pleural effusion classification (PE).

Linear classifiers indicate the usefulness of pretrained backbones, as the only trainable weights for supervised learning are those belonging to the perceptron head. Table V reports the test set performance of linear classifiers for each task and data augmentation pipeline. On the private dataset, the AugUS-D and BYOL pipelines performed comparably well on the AB task. AugUS-D attained greater performance metrics than the BYOL pipeline on PE. To provide a visual perspective on linear classifier performance, we produced two-dimensional t-

TABLE IV
A COMPARISON OF ABLATED VERSIONS OF THE BYOL AND AUGUS-O PIPELINE WITH ONE EXCLUDED TRANSFORMATION VERSUS THE ORIGINAL PIPELINES. MODELS WERE PRETRAINED ON THE LUSDATA UNLABELED SET AND EVALUATED ON TWO DOWNSTREAM CLASSIFICATION TASKS – AB AND PE. PERFORMANCE IS EXPRESSED AS MEAN AND MEDIAN TEST AUC FROM 10-FOLD CROSS-VALIDATION ACHIEVED BY A LINEAR CLASSIFIER TRAINED ON THE FEATURE VECTORS OF A FROZEN BACKBONE.

Pipeline	Omitted	AB		PE	
		Mean	Median	Mean	Median
BYOL	None (baseline)	0.978	0.978	0.852	0.845
	<i>B00</i>	0.864	0.873 [†]	0.695	0.707 [†]
	<i>B01</i>	0.976	0.974	0.848	0.856
	<i>B02</i>	0.975	0.975 [†]	0.840	0.842 [†]
	<i>B03</i>	0.978	0.978	0.849	0.846
	<i>B04</i>	0.976	0.975	0.840	0.842
	<i>B05</i>	0.977	0.977	0.851	0.853
	None (baseline)	0.956	0.959	0.828	0.837
	<i>U00</i>	0.958	0.957	0.831	0.839
	<i>U01</i>	0.952	0.952	0.835	0.838
AugUS-O	<i>U02</i>	0.965	0.967 ^{\$}	0.840	0.851
	<i>U03</i>	0.950	0.951 [†]	0.825	0.827
	<i>U04</i>	0.957	0.958	0.831	0.836
	<i>U05</i>	0.953	0.952	0.839	0.845
	<i>U06</i>	0.961	0.959	0.829	0.833
	<i>U07</i>	0.959	0.960	0.838	0.856
	<i>U08</i>	0.961	0.966 ^{\$}	0.834	0.849
	<i>U09</i>	0.962	0.967 ^{\$}	0.838	0.845
	<i>U10</i>	0.956	0.959	0.826	0.838
	<i>U11</i>	0.937	0.939 [†]	0.825	0.823

[†] Median is significantly less than baseline.

^{\$} Median is significantly greater than baseline.

TABLE V
TEST SET METRICS FOR LINEAR CLASSIFICATION FOR EACH OF THE AB AND PE TASKS.

Task	Weights	Pipeline	Accuracy	Precision	Recall	AUC
AB	SimCLR	BYOL	0.932	0.951	0.819	0.970
	SimCLR	AugUS-O	0.910	0.939	0.756	0.953
	SimCLR	AugUS-D	0.931	0.947	0.820	0.971
	ImageNet	-	0.898	0.894	0.758	0.949
PE	SimCLR	BYOL	0.801	0.783	0.788	0.893
	SimCLR	AugUS-O	0.810	0.800	0.785	0.865
	SimCLR	AugUS-D	0.816	0.808	0.789	0.897
	ImageNet	-	0.806	0.774	0.820	0.884

SNE embeddings of the feature vectors outputted by pretrained backbones. Shown in Fig. 5, the separability of the visual representations is consistent with linear classifier performance. For AB, AugUS-O exhibits worse separation between classes. On PE, AugUS-D appeared to have the most demarcated class separation.

We fine-tuned the pretrained models, allowing the backbone’s weights to be trainable in addition to the model head. Table VI gives the test set performance of the fine-tuned classifiers. We observed similar performance differences among the different augmentation pipelines, but note some additional findings. The model pretrained using AugUS-O on LUSData performed comparably against the other pipelines on AB, but exhibited extremely poor performance on the PE test set. Although it may appear that this model may have overfit to the training set, examination of training metrics revealed

TABLE VI
TEST SET METRICS FOR CLASSIFIERS FINE-TUNED FOR EACH OF THE AB AND PE TASKS.

Task	Initial Weights	Pipeline	Accuracy	Precision	Recall	AUC
AB	SimCLR	BYOL	0.941	0.951	0.850	0.970
	SimCLR	AugUS-O	0.939	0.938	0.859	0.968
	SimCLR	AugUS-D	0.931	0.960	0.809	0.962
	Random	-	0.883	0.794	0.834	0.938
	ImageNet	-	0.911	0.872	0.830	0.953
PE	SimCLR	BYOL	0.766	0.713	0.863	0.882
	SimCLR	AugUS-O	0.487	0.479	0.685	0.557
	SimCLR	AugUS-D	0.802	0.782	0.818	0.884
	Random	-	0.703	0.733	0.607	0.767
	ImageNet	-	0.708	0.640	0.907	0.845

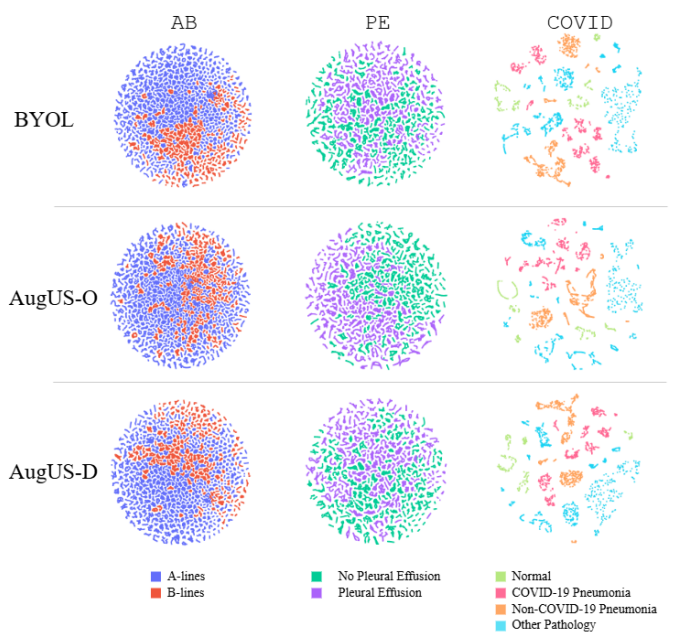


Fig. 5. Two-dimensional t-SNE projections for test set feature vectors produced by SimCLR-pretrained backbones, for all tasks and data augmentation pipelines.

that training and validation metrics were close, with validation set AUC having been evaluated as 0.861. Nonetheless, fine-tuned models that were pretrained with the BYOL and AugUS-O pipelines yielded strong performance on both tasks in LUSData.

Fine-tuned classifiers for the AB and PE tasks were also evaluated on the external portion of the LUSData test set. Most classifiers exhibited degraded performance on external data, compared to the local test set. Overall, the relative performance of the classifiers on the external test set was reflective of their performance on local test data. Unlike the local test evaluation, the network trained from scratch performed comparably to the SimCLR-pretrained models that utilized the AugUS-O and AugUS-D pipelines; however, the SimCLR-pretrained model that utilized the BYOL pipeline achieved the greatest test AUC by a margin of 0.029. On the PE task, the classifier originating from the same pretrained model that utilized BYOL achieved the greatest AUC by a margin of 0.018. Similar to the local test set, the pretrained models that incorporated the BYOL and

TABLE VII

EXTERNAL TEST SET METRICS FOR CLASSIFIERS FINE-TUNED FOR THE AB AND PE TASKS.

Task	Initial Weights	Pipeline	Accuracy	Precision	Recall	AUC
AB	SimCLR	BYOL	0.751	0.961	0.556	0.883
	SimCLR	AugUS-O	0.734	0.960	0.523	0.850
	SimCLR	AugUS-D	0.712	0.934	0.500	0.854
	Random	-	0.748	0.885	0.606	0.853
	ImageNet	-	0.718	0.903	0.527	0.814
PE	SimCLR	BYOL	0.805	0.838	0.861	0.898
	SimCLR	AugUS-O	0.572	0.649	0.717	0.536
	SimCLR	AugUS-D	0.800	0.904	0.768	0.879
	Random	-	0.700	0.850	0.643	0.804
	ImageNet	-	0.776	0.775	0.914	0.840

AugUS-D pipeline achieved the greatest test AUC, while the pretrained model that utilized AugUS-O performed the worst.

C. Diagnostic Classification Task Evaluation

Models pretrained on LUSData were also evaluated on the COVID-19 multi-class problem (COVID). Unlike the AB and PE tasks, COVID is a diagnostic task that involves global image understanding, as the relationship between objects is pertinent. Multiple findings on lung ultrasound have been observed in the context of COVID-19 pneumonia, including B-lines, pleural line abnormalities, and consolidation [38].

Linear classifiers were trained on the COVID training set and evaluated on the COVID test set. As shown in Table VIII, AugUS-O was observed to have the greatest test multiclass AUC, which was considered the primary metric of interest. Looking at the *t*-SNE visualizations in Fig. 5, AugUS-O corresponds to the only visualization where the representations for the COVID-19 Pneumonia and non-COVID-19 Pneumonia classes are clustered together.

Table IX provides test metrics for fine-tuned COVID classifiers. Again, AugUS-O exhibited the best performance. Moreover, fine-tuned models generally performed worse than the linear classifiers trained on feature vectors from SSL-pretrained models; they likely suffered from overfitting, as COVIDx-US is a smaller dataset.

Unlike the AB and PE tasks, models trained for COVID were pretrained using the LUSData dataset. We repeated the linear classification and fine-tuning experiments using models pretrained on the COVIDx-US training set. Tables VIII and IX respectively report the results of linear and fine-tuning evaluations. As was observed for backbones pretrained on LUSData, pretraining with the AugUS-O pipeline resulted in the greatest test set AUC.

The trends observed for the COVID task are different than those observed for the AB and PE tasks. Regardless of the augmentation pipeline, SimCLR-pretrained weights resulted in better performance than ImageNet-pretrained or random weight initialization. On object classification tasks, models pretrained using the BYOL and AugUS-D pipelines performed the best. However, on the diagnostic COVID task, AugUS-O performed best. Recall that AugUS-O was designed to retain semantic information, while both BYOL and AugUS-D contain the very impactful crop & resize (C&R) transform that

TABLE VIII

TEST SET PERFORMANCE FOR LINEAR CLASSIFIERS TRAINED FOR THE COVID TASK. BINARY METRICS ARE AVERAGES ACROSS CLASSES.

Pretraining Dataset	Initial Weights	Pipeline	Accuracy	Precision	Recall	AUC
LUSData	SimCLR	BYOL	0.454	0.371	0.413	0.784
	SimCLR	AugUS-O	0.560	0.431	0.513	0.836
	SimCLR	AugUS-D	0.487	0.348	0.447	0.713
COVIDx-US	SimCLR	BYOL	0.498	0.582	0.501	0.781
	SimCLR	AugUS-O	0.557	0.506	0.543	0.820
	SimCLR	AugUS-D	0.540	0.400	0.491	0.760
-	ImageNet	-	0.503	0.304	0.451	0.699

TABLE IX

TEST SET PERFORMANCE FOR FINE-TUNED CLASSIFIERS TRAINED FOR THE COVID TASK. BINARY METRICS ARE AVERAGES ACROSS CLASSES.

Pretraining Dataset	Initial Weights	Pipeline	Accuracy	Precision	Recall	AUC
LUSData	SimCLR	BYOL	0.381	0.259	0.365	0.753
	SimCLR	AugUS-O	0.557	0.428	0.509	0.836
	SimCLR	AugUS-D	0.465	0.321	0.430	0.744
COVIDx-US	SimCLR	BYOL	0.450	0.540	0.464	0.770
	SimCLR	AugUS-O	0.517	0.483	0.510	0.814
	SimCLR	AugUS-D	0.526	0.384	0.479	0.672
-	Random	-	0.423	0.327	0.401	0.534
-	ImageNet	-	0.502	0.305	0.457	0.698

can obscure large portions of the image. Object classification tasks require scale invariance, which is enforced by applying C&R during SSL pretraining. Diagnostic tasks, on the other hand, require global image context for interpreters to make a decision, which is preserved best by the AugUS-O pipeline.

D. Object Detection Task Evaluation

Recall that the PL task is an object detection problem geared toward localizing the pleural line artifact. We evaluated the pretrained models on PL to explore whether the trends observed for object-centric lung US classification tasks would hold for an object detection task, where locality understanding is explicit. We considered two evaluation settings: one in which the pretrained backbones weights were held constant, and another in which the backbone's weights were trainable. Table X reports the average precision at a 50% intersection over union threshold (AP@50) evaluated on the LUSData test set. When the backbone weights were frozen, SimCLR pretraining with BYOL and AugUS-D resulted in the greatest test AP@50. These trends reflected the results observed for AB and PE classification, which both require object recognition. However, when training end-to-end, models trained from scratch matched the performance of pretrained models.

E. Label Efficiency Assessment

Experiments were conducted to test the robustness of pretrained models in settings where few labeled samples are available. The experiment was conducted only for the AB and PE classification tasks because there were enough unique videos and patients in the training set to create several disjoint subsets.

TABLE X

LUSDATA LOCAL TEST SET AP@50 FOR THE PL TASK OBSERVED FOR SSD MODELS WHOSE BACKBONES WERE PRETRAINED USING DIFFERENT DATA AUGMENTATION PIPELINES.

Backbone	Initial Weights	Pipeline	AP@50
Frozen	SimCLR	BYOL	0.136
	SimCLR	AugUS-O	0.047
	SimCLR	AugUS-D	0.108
	Random	-	0.012
	ImageNet	-	0.043
Trainable	SimCLR	BYOL	0.136
	SimCLR	AugUS-O	0.141
	SimCLR	AugUS-D	0.143
	Random	-	0.142
	ImageNet	-	0.127

Backbones were fine-tuned on 20 subsets of approximately 5% of the LUSData training set, split by patient, yielding 20 performance estimates for low-label settings. Splitting was conducted at the patient level to heighten the difficulty of the task and to limit dependence between subsets. Baseline estimates without SSL pretraining were obtained via initialization with random weights and with ImageNet-pretrained weights, resulting in five different performance conditions. Friedman’s Test indicated that there were significant differences among the median test AUCs across conditions, for both the AB and PE tasks. Post-hoc Wilcoxon Sign-Rank Tests were then conducted for each pair of conditions, using the Bonferroni correction with a family-wise error rate of $\alpha = 0.05$. The median test AUCs of SimCLR-pretrained models were significantly greater than those initialized with random or ImageNet-pretrained weights for both the AB and PE tasks. All medians were significantly different for AB, except for the SimCLR-pretrained models using the BYOL and AugUS-D pipelines, which achieved the greatest performance. Notably, these pipelines both utilize the crop and resize transformation. No significant differences were observed between any of the SimCLR-pretrained models for PE. Appendix R provides the test statistics for the above comparisons.

F. Impact of Semantic-Preserving Preprocessing

As outlined in Section III-B, all US images were cropped to the smallest rectangle enclosing the FOV because the areas outside the FOV are bereft of information. Since pipelines containing the crop and resize transformation (C&R) would be more likely to result in positive pairs that do not cover the FOV, it was hypothesized that cropping to the FOV as a preprocessing step would result in stronger pretrained backbones. To investigate the effect of this semantics-preserving preprocessing step, we pretrained backbones on LUSData using each data augmentation pipeline and evaluated them on the AB, AB, and COVID tasks. Table XI compares the performance of each backbone with and without the preprocessing step. Performance on the AB task did not change. However, test AUC on both the PE and COVID tasks was consistently lower when the semantics-preserving preprocessing was not applied. Note that greatly less labelled data is available for PE and COVID than for AB. Based on these experiments, FOV

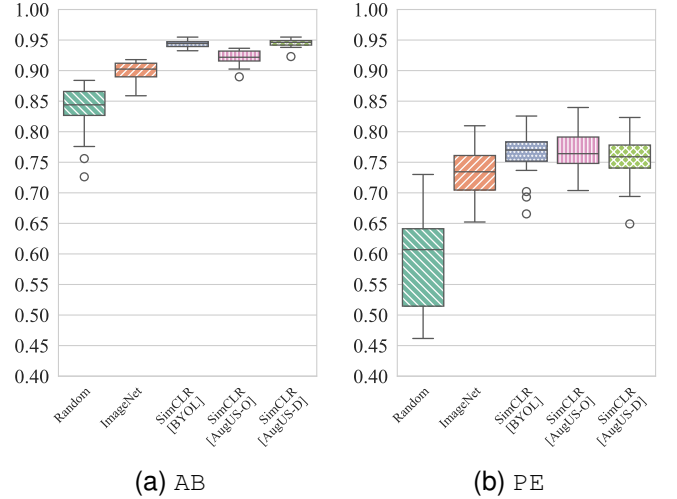


Fig. 6. Distribution of test AUC for classifiers trained on disjoint subsets of 5% of the patients in the training partition of the private dataset

TABLE XI
TEST SET AUC FOR SIMCLR-PRETRAINED MODELS WITH AND WITHOUT SEMANTICS-PRESERVING PREPROCESSING. RESULTS ARE REPORTED FOR LINEAR CLASSIFIERS AND FINE-TUNED MODELS.

Task	Pipeline / Preprocessing	Linear classifier		Fine-tuned	
		\times	\checkmark	\times	\checkmark
AB	BYOL	0.971	0.970	0.971	0.970
	AugUS-O	0.950	0.953	0.926	0.968
	AugUS-D	0.971	0.971	0.961	0.962
PE	BYOL	0.873	0.893	0.869	0.882
	AugUS-O	0.846	0.865	0.522	0.557
	AugUS-D	0.867	0.897	0.864	0.884
COVID	BYOL	0.742	0.784	0.724	0.753
	AugUS-O	0.793	0.836	0.805	0.836
	AugUS-D	0.585	0.713	0.737	0.744

cropping is a valuable semantics-preserving preprocessing step for multiple LUS classification tasks.

G. Impact of the Cropping in Object Classification Tasks

The leave-one-out analysis for transformations exhibited the striking finding that crop and resize (C&R) was the most effective transformation in the BYOL pipeline for the two object classification tasks: AB and PE. Moreover, both pipelines containing C&R resulted in the greatest downstream test performance on AB and PE. Ordinarily, crops are taken at random locations in an image, with areas between 8% and 100% of the original image’s area. Aggressive crops can create situations in which positive pairs do not contain the same objects of interest. For example, Fig. 7 shows how C&R could produce a positive pair where the views would possess different labels. Despite this, the results indicated that pipelines containing C&R led to improved performance for the object-centric AB and PE tasks. The exceptional influence of C&R warranted further investigation into its hyperparameters.

We investigated the impact of the minimum crop area, c , as a hyperparameter. Models were pretrained with the AugUS-D pipeline, using values for c in the range $[0.05, 0.9]$. Linear

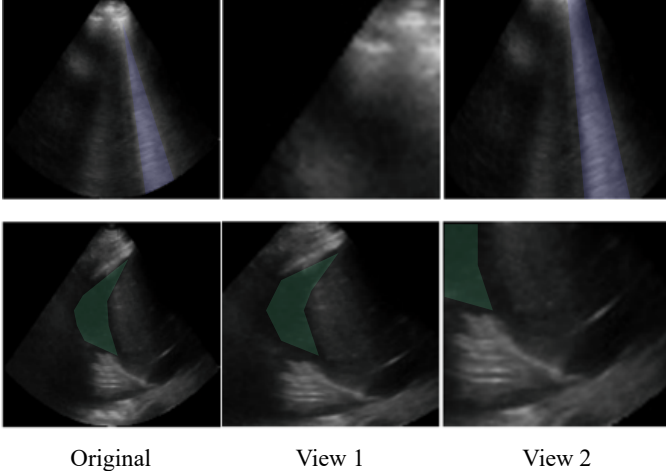


Fig. 7. Examples of how the random crop and resize transformation (B00) can reduce semantic information. Original images are on the left, and two random crops of the image are on the right. **Top:** The original image contains a B-line (purple), which is visible in View 2, but not in View 1. **Bottom:** The original image contains a pleural effusion (green), which is visible in View 1, but is largely obscured in View 2.

evaluation was conducted for the AB and PE tasks. As shown in Fig. 8, smaller values of c yielded better performance, peaking at $c \approx 0.1$. The default assignment of $c = 0.08$ was already a reasonable choice for these two tasks. Additional experiments elucidating the effects of C&R hyperparameters can be found in Appendix R.

Another concern with C&R is that it could result in crops covering the black background on images with a convex FOV. Despite the semantics-preserving preprocessing (described in Section 2), the top left and right corners of such images provide no information. To characterize the robustness of pretraining under these circumstances, we repeated the experiments sweeping over $c \in [0.05, 0.9]$, but first applied the probe type change transformation (i.e., U00) to every convex FOV. Thus, all inputs to the model were linear FOVs devoid of non-semantic background. A by-product of this transformation is that the near fields of convex images are horizontally stretched. As seen in Fig. 8, this change resulted in a slight decrease in performance for both the AB and PE tasks. Evidently, the detriment of spatial distortion outweighed the benefit of guaranteeing that crops were positioned over semantic regions.

Overall, it is clear that aggressive C&R is beneficial for distinguishing between A-lines and B-lines and detecting pleural effusions on lung US. Both are object-centric classification tasks. Even though some crops may not contain the object, the backbone would be exposed to several paired instances of transformed portions of objects during pretraining, potentially facilitating texture and shape recognition. Conversely, solving diagnostic tasks such as COVID requires a holistic assessment of the FOV, wherein the co-occurrence of objects is contributory to the overall impression.

V. CONCLUSION

This study proposed data augmentation and preprocessing strategies for self-supervised learning in ultrasound. A com-

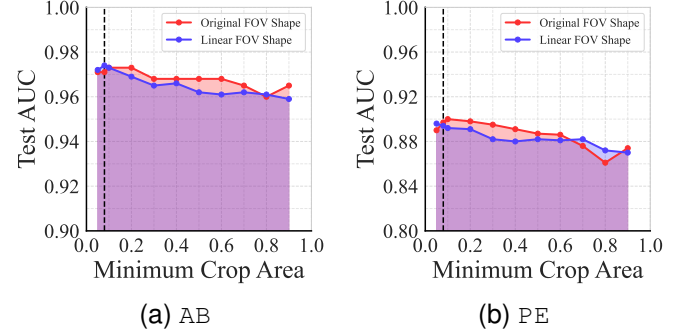


Fig. 8. Test set AUC for linear classifiers trained on the representations outputted by pretrained backbones. Each backbone was pretrained using AugUS-D with different values for the minimum crop area, c . Results are provided for models pretrained with the original ultrasound FOV, along with images transformed to linear FOV only. The dashed line indicates the default value of $c = 0.08$.

monly employed baseline pipeline (BYOL) was compared to a handcrafted semantics-preserving pipeline (AugUS-O) and a hybrid pipeline (AugUS-D) composed from the first two. Evaluation on lung US interpretation tasks revealed a dichotomy between the utility of the pipelines. Pipelines featuring the cropping transformation (BYOL and AugUS-D) were most useful for object classification and detection tasks in LUS. On the other hand, AugUS-O – designed to preserve semantics in LUS – resulted in the greatest performance on a diagnostic task that required global context. Additionally, US field of view cropping was found to be a beneficial preprocessing step for multiple lung US classification tasks, regardless of the data augmentation strategy. Based on the results, practitioners should use semantics-preserving preprocessing during pre-training. Regarding data augmentation, semantics-preserving transformations should be considered for tasks requiring holistic interpretation of images, cropping-based transformations should be leveraged for object-centric downstream tasks.

Some limitations are acknowledged in this study. For example, SimCLR was the only SSL objective that was investigated, and all downstream tasks were confined to the lung. Moreover, some of the transformations introduced in this work constitute computationally expensive preprocessing steps, as they are applied with nonzero probability to each image.

Future work should apply this study’s methods to assess the impact of data augmentation pipelines for US diagnostic tasks outside of the lung and for other SSL methods. Future studies could also compare data augmentation strategies for localization and segmentation downstream tasks in ultrasound.

APPENDIX

This section provides further details regarding the composition of the LUSData and COVIDx-US datasets, stratified by different attributes. Table XII provides a breakdown of the characteristics of the unlabelled data, training set, validation set, local test set, and external test set. As can be seen in the table, the external test set's manufacturer and probe type distributions differ greatly from those in the local test set. As such, the external test set constitutes a meaningful assessment of generalizability for models trained using the LUSData dataset. Table XIII provides similar information for the COVIDx-US dataset [23]. Note that the probe types listed in Tables XII and XIII are predictions produced by a ultrasound cleaning software (UltraMask, Deep Breathe Inc., London, ON, Canada) – not from meta-data accompanying the examinations.

We aimed to examine relative runtime differences between the transformations used in this study. Runtime estimates were obtained for each transformation in the BYOL and AugUS-v1 pipelines. Estimates were calculated by conducting the transformation 1000 times using the same image. The experiments were run on a system with an Intel i9-10900K CPU at 3.7 GHz. Python 3.11 was utilized, and the transforms were written using PyTorch version 2.2.1 and TorchVision 0.17.1. Note that runtime may vary considerably depending on the software environment and underlying hardware.

We investigated the data augmentation pipeline from the BYOL study [13]. More specifically, we adopted the symmetric version from the VICReg paper [39], which uses the same transformations and probabilities for each of the two branches in the joint embedding architecture. The transformations and their parameters are widely adopted; nevertheless, we detail their operation and parameters below.

A. Crop and Resize (B00)

A rectangular crop of the input image is designated at a random location. The area of the cropped region is sampled from the uniform distribution $\mathcal{U}(0.08, 1)$. The cropped region's aspect ratio is sampled from the uniform distribution $\mathcal{U}(0.75, 1.33)$. Its width and height are calculated accordingly. The cropped region is then resized to the original image dimension.

B. Horizontal Reflection (B01)

The image is reflected about the central vertical axis.

C. Color Jitter (B02)

The brightness, contrast, saturation, and hue of the image are modified. The brightness change factor, contrast change factor, saturation change factor, and hue change factor are sampled from $\mathcal{U}(0.6, 1.4)$, $\mathcal{U}(0.6, 1.4)$, $\mathcal{U}(0.8, 1.2)$, and $\mathcal{U}(-0.1, 0.1)$, respectively.

D. Conversion to Grayscale (B03)

Images are converted to grayscale. The output images has three channels, such that each channel has the same pixel intensity.

E. Gaussian Blur (B04)

The image is denoised using a Gaussian blur with kernel size 13 and standard deviation sampled uniformly at random from $\mathcal{U}(0.1, 2)$. Note that in the original pipeline, the kernel size was set to 23 and 224×224 images were used. We used 128×128 images; as such, we selected a kernel size that covers a similar fraction of the image.

F. Solarization (B05)

All pixels with intensity of 128 or greater are inverted. Note that the inputs are unsigned 8-bit images.

In this section, we provide details on the set of transformations that comprise AugUS-v1.

Several of the transformations operate on the pixels contained within the ultrasound (US) beam. As such, the geometrical form of the beam was required to perform some transformations. We adopted the same naming convention for the vertices of the US beam as Kim *et al.* [40]. Let p_1, p_2, p_3 , and p_4 represent the respective locations of the top left, top right, bottom left, and bottom right vertices, and let $\langle x_i, y_i \rangle$ be the x- and y-coordinates of p_i in image space. For convex beam shapes, we denote the intersection of lines $\overleftrightarrow{p_1p_3}$ and $\overleftrightarrow{p_2p_4}$ as p_0 . Fig. 9 depicts the arrangement of these points for each of the three main US beam shapes: linear, curvilinear, and phased array. A software tool was used to estimate the beam vertices and probe type for all videos in each dataset (UltraMask, Deep Breathe Inc., Canada).

G. Probe Type Change (U00)

To produce a transformed ultrasound image with a different beam shape, a mapping that gives the location of pixels in the original image for each coordinate in the new image is calculated. Concretely, the function $f : \mathbb{R}^2 \rightarrow [-1, 1]^2$ returns the coordinates of the point in the original image that corresponds to a point in the transformed image. Note that $(-1, -1)$ corresponds to the top left of the original image. Pixel intensities in the transformed image are interpolated according to their corresponding location in the original image.

Algorithm 1 details the calculation of $f_{\ell \rightarrow c}$ for converting linear beams to convex beams with a random radius factor $\rho \sim \mathcal{U}(1, 2)$, along with new beam vertices. Similarly, curvilinear and phased array beam shapes are converted to linear beam shapes. Algorithm 2 details the calculation of the mapping $f_{c \rightarrow \ell}$ that transforms convex beam shapes to linear shapes, along with calculations for the updated named coordinates. To ensure that no aspects of the old beam remain on the image, bitmask $M' \in \{0, 1\}^{h \times w}$ is produced using the new named coordinates.

Since the private dataset was resized to square images that exactly encapsulated the beam, images are resized to match their original aspect ratios to ensure that the sectors were circular. They are then resized to their original dimensions following the transformation.

H. Convexity Change (U01)

To mimic an alternative convex beam shape with a different θ_0 , a mapping is calculated that results in a new beam shape

TABLE XII

CHARACTERISTICS OF THE ULTRASOUND VIDEOS IN THE LUSDATA DATASET. THE NUMBER OF VIDEOS POSSESSING KNOWN VALUES FOR A VARIETY OF ATTRIBUTES ARE DISPLAYED. PERCENTAGES OF THE TOTAL IN EACH SPLIT ARE PROVIDED AS WELL, BUT SOME DO NOT SUM TO 100 DUE TO ROUNDING.

	Local				External
	Unlabeled	Train	Validation	Test	Test
Probe Type					
Phased Array	50 769 (85.6%)	5146 (90.6%)	1051 (88.8%)	1062 (85.0%)	586 (63.4%)
Curved Linear	6601 (11.1%)	439 (7.7%)	108 (9.1%)	167 (13.4%)	92 (9.9%)
Linear	1939 (3.3%)	94 (1.7%)	25 (2.1%)	20 (1.6%)	247 (26.7%)
Manufacturer					
Sonosite	53 663 (90.5%)	4386 (77.2%)	848 (71.6%)	963 (77.1%)	626 (67.7%)
Mindray	4045 (6.8%)	847 (14.9%)	216 (18.2%)	153 (12.2%)	55 (5.9%)
Philips	66 (0.1%)	50 (0.9%)	6 (0.5%)	11 (0.9%)	244 (26.4%)
Esaote	233 (0.4%)	4 (0.1%)	0 (0.0%)	0 (0.0%)	0 (0.0%)
GE [§]	10 (0.0%)	0 (0.0%)	0 (0.0%)	0 (0.0%)	0 (0.0%)
Depth (cm)					
Mean [STD]	14.3 [4.5]	13.0 [3.8]	13.1 [3.7]	12.7 [3.8]	11.1 [4.8]
Unknown	1606 (2.7%)	407 (7.2%)	115 (9.7%)	122 (9.8%)	0 (0.0%)
Acquisition Environment					
ICU [†]	43 839 (73.9%)	3722 (65.5%)	706 (59.6%)	727 (58.2%)	0 (0.0%)
ER [‡]	13 280 (22.4%)	760 (13.4%)	206 (17.4%)	253 (20.3%)	0 (0.0%)
Ward	2033 (3.4%)	173 (3.0%)	25 (2.1%)	49 (3.9%)	0 (0.0%)
Urgent Care	129 (0.2%)	3 (0.1%)	0 (0.0%)	1 (0.1%)	0 (0.0%)
Unknown	28 (0.0%)	1021 (18.0%)	247 (20.9%)	219 (17.5%)	925 (100.0%)
Patient Sex					
Male	30 300 (51.1%)	2963 (52.2%)	607 (51.3%)	588 (47.1%)	0 (0.0%)
Female	20 809 (35.1%)	1793 (31.6%)	325 (27.4%)	412 (33.0%)	0 (0.0%)
Unknown	8200 (13.8%)	923 (16.3%)	252 (21.3%)	249 (19.9%)	925 (100.0%)
Patient Age					
Mean [STD]	62.3 [20.0]	63.3 [16.5]	62.0 [18.4]	62.8 [17.3]	—
Unknown	53 (0.1%)	1029 (18.2%)	247 (20.9%)	219 (17.5%)	925 (100.0%)
Total	59 309	5679	1184	1249	925

[§] General Electric

[†] Intensive Care Unit

[‡] Emergency Room

Algorithm 1 Compute a point mapping for linear to curvilinear beam shape, along with new beam vertices

Require: Beam vertices p_1, p_2, p_3, p_4 ; radius factor ρ ; coordinate maps $\mathbf{x} = \mathbf{1}_{h \times 1}[0, 1, \dots, w - 1]$ and $\mathbf{y} = [0, 1, \dots, h - 1]^T \mathbf{1}_{1 \times w}$

- 1: $r_b \leftarrow \rho(y_3 - y_1)$ \triangleright Bottom sector radius
- 2: $x'_0 \leftarrow \max(x_3, 0) + (x_4 - x_3)/2$
- 3: $y'_0 \leftarrow y_3 - r_b$ \triangleright Intersection of lateral bounds
- 4: $y'_1 = y'_2 \leftarrow y_1$
- 5: $y'_3 = y'_4 \leftarrow y'_0 + \sqrt{r_b^2 - (x'_0 - x_1)^2}$
- 6: $x'_1 \leftarrow x'_0 - (y_1 - y'_0)(x'_0 - x_3)/(y'_3 - y'_0)$
- 7: $x'_2 \leftarrow 2x'_0 - x'_1$
- 8: $r_t \leftarrow \sqrt{(x'_0 - x'_1)^2 + (y_1 - y'_0)^2}$ \triangleright Top sector radius
- 9: $\phi \leftarrow \text{atan2}(\mathbf{x} - x_0, \mathbf{y} - y_0)$ \triangleright Angle with vertical
- 10: $\mathbf{f}_{\ell \rightarrow c} \leftarrow \begin{pmatrix} \frac{\phi + (x_i - w/2)/w}{|\phi| y'_3 |0|} \\ \frac{2\sqrt{(x'_0 - \mathbf{x})^2 + (y'_0 - \mathbf{y})^2} - r_t}{r_b - r_t} - 1 \end{pmatrix}$
- 11: **return** $\mathbf{f}_{\ell \rightarrow c}, p'_1, p'_2, p'_3, p'_4$

Algorithm 2 Compute a point mapping for convex to linear beam shape, along with new beam vertices

Require: Beam vertices p_1, p_2, p_3, p_4 ; point of intersection p_0 ; angle of intersection θ_0 ; width fraction $\omega \in [0, 1]$; coordinate maps $\mathbf{x} = \mathbf{1}_{h \times 1}[0, 1, \dots, w - 1]$ and $\mathbf{y} = [0, 1, \dots, h - 1]^T \mathbf{1}_{1 \times w}$

- 1: $r_b \leftarrow \sqrt{(x'_0 - x_3)^2 + (y'_0 - y_3)^2}$ \triangleright Bottom sector radius
- 2: $x'_1 = x'_3 \leftarrow x_0 - \omega w/2$
- 3: $x'_2 = x'_4 \leftarrow x_0 + \omega w/2$
- 4: $y'_1 = y'_2 \leftarrow y_1$
- 5: $y'_3 = y'_4 \leftarrow y_0 + r_b$
- 6: $\phi \leftarrow \theta_0((\mathbf{x} - x_3)/(x_4 - x_3) - \frac{1}{2})$ \triangleright Angle with vertical
- 7: $\mathbf{y}_n \leftarrow (\mathbf{y} - y_1)/(y_3 - y_1)$ \triangleright Normalized y-coordinates
- 8: **if** Probe type is curvilinear **then**
- 9: $r_t \leftarrow \sqrt{(x'_0 - x_1)^2 + (y'_0 - y_1)^2}$ \triangleright Top sector radius
- 10: **else**
- 11: $r_t \leftarrow (y_1 - y_0)/\cos(\phi/w)$ \triangleright Top line segment
- 12: **end if**
- 13: $\mathbf{f}_{c \rightarrow \ell} \leftarrow \begin{pmatrix} x_0 + \sin(\phi/w)(r_t + \mathbf{y}_n(r_b - r_t)) \\ y_0 + \cos(\phi/w)(r_t + \mathbf{y}_n(r_b - r_t)) \end{pmatrix}$
- 14: **return** $\mathbf{f}_{c \rightarrow \ell}, p'_1, p'_2, p'_3, p'_4$

TABLE XIII
CHARACTERISTICS OF THE ULTRASOUND VIDEOS IN THE COVIDX-US DATASET. THE NUMBER OF VIDEOS POSSESSING KNOWN VALUES FOR A VARIETY OF ATTRIBUTES ARE DISPLAYED. PERCENTAGES OF THE TOTAL IN EACH SPLIT ARE PROVIDED AS WELL, BUT SOME DO NOT SUM TO 100 DUE TO ROUNDING.

	Train	Validation	Test
Probe Type			
Phased Array	55 (32.5%)	18 (42.9%)	11 (35.5%)
Curved Linear	83 (49.1%)	13 (31.0%)	10 (32.3%)
Linear	31 (18.3%)	11 (26.2%)	10 (32.3%)
Patient Sex			
Male	33 (19.5%)	15 (35.7%)	7 (22.6%)
Female	18 (10.7%)	3 (7.1%)	3 (9.7%)
Unknown	118 (69.8%)	24 (57.1%)	21 (67.7%)
Patient Age			
Mean [STD]	36.6 [14.6]	47.6 [18.9]	52.9 [21.1]
Unknown	127 (75.1%)	22 (52.4%)	20 (64.5%)
Total	169	42	31

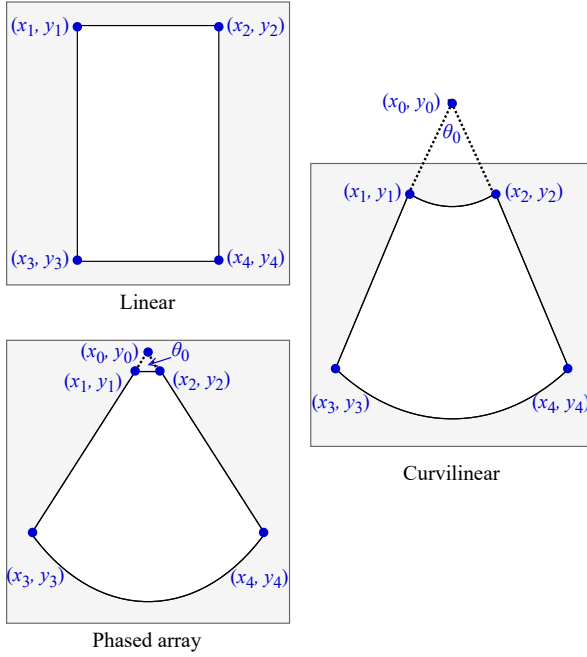


Fig. 9. Location of the named beam vertices for each of the three main beam shapes in US imaging

wherein p_0 is translated vertically. A new value for the width of the top of the beam is randomly calculated, facilitating the specification of a new p_0 . Given the new p_0 , a pixel map $\mathbf{f}_{c \rightarrow c'}$ is computed according to Algorithm 3. Similar to the probe type change transformation, pixel intensities at each coordinate in the transformed image are interpolated according to the corresponding coordinate in the original image returned by $\mathbf{f}_{c \rightarrow c'}$.

I. Wavelet Denoising (U02)

Following the soft thresholding method by Birgé and Masart [25], we apply a wavelet transform, conduct thresholding,

Algorithm 3 Compute a point mapping from an original to a modified convex beam shape.

Require: Beam vertices p_1, p_2, p_3, p_4 ; point of intersection p_0 ; angle of intersection θ_0 ; new top width w' ; coordinate maps $\mathbf{x} = \mathbf{1}_{h \times 1}[0, 1, \dots, w - 1]$ and $\mathbf{y} = [0, 1, \dots, h - 1]^T \mathbf{1}_{1 \times w}$

- 1: $s \leftarrow w'(x_4 - x_3)/(x_2 - x_1)$ \triangleright Scale change for top
- 2: $x'_1 \leftarrow x_0 - s(x_0 - x_1)$
- 3: $x'_2 \leftarrow x_0 + s(x_2 - x_0)$
- 4: $y'_1 = y'_2 \leftarrow y_1$
- 5: $y'_3 = y'_4 \leftarrow y_3$
- 6: $\theta'_0, p'_0 \leftarrow \text{angle, point of intersection of } \overleftrightarrow{p'_1 p'_3} \text{ and } \overleftrightarrow{p'_2 p'_4}$
- 7: $r_b \leftarrow \sqrt{(x_0 - x_3)^2 + (y_0 - y_3)^2}$ \triangleright Current bottom radius
- 8: $r'_b \leftarrow \sqrt{(x'_0 - x'_3)^2 + (y'_0 - y'_3)^2}$ \triangleright New bottom radius
- 9: $r_t \leftarrow \sqrt{(x_0 - x_1)^2 + (y_0 - y_1)^2}$ \triangleright Current top radius
- 10: $r'_t \leftarrow \sqrt{(x'_0 - x'_1)^2 + (y'_0 - y'_1)^2}$ \triangleright New top radius
- 11: $\phi' \leftarrow \text{atan2}(\mathbf{x} - x'_0, \mathbf{y} - y'_0)$
- 12: $\mathbf{r}' \leftarrow \sqrt{(x'_0 - \mathbf{x})^2 + (y'_0 - \mathbf{y})^2}$
- 13: $\mathbf{r}' \leftarrow (\mathbf{r}' - r'_t)(r_b - r_t)/(r'_b - r'_t) + r_t$
- 14: $\mathbf{f}_{c \rightarrow c'}(x, y) \leftarrow \begin{pmatrix} x_0 + \mathbf{r}' \sin(\phi' \theta_0 / \theta'_0) \\ y_0 + \mathbf{r}' \cos(\phi' \theta_0 / \theta'_0) \end{pmatrix}$
- 15: **return** $\mathbf{f}_{c \rightarrow c'}, p'_1, p'_2, p'_3, p'_4$

then apply the inverse wavelet transform. The mother wavelet is randomly chosen from a set, and the sparsity parameter α is sampled from a uniform distribution. We use $J = 3$ levels of wavelet decomposition and set the decomposition level $J_0 = 2$. We designated Daubechies wavelets $\{db2, db5\}$ as the set of mother wavelets, which is a subset of those identified by Vilimek *et al.*'s assessment [27] as most suitable for denoising US images.

J. Contrast-Limited Adaptive Histogram Equalization (U03)

Contrast-limited adaptive histogram equalization is applied to the input image. The transformation enhances low-contrast regions of ultrasound images while avoiding excessive noise amplification. We found that CLAHE enhances artifact The

tiles are 8×8 regions of pixels. The clip limit is sampled from the uniform distribution $\mathcal{U}(30, 50)$.

K. Gamma Correction (U04)

The pixel intensities of the image are nonlinearly modified. Pixel intensity I is transformed as follows:

$$I' \leftarrow 255 \left(\frac{I}{255} \right)^\gamma \quad (1)$$

where $\gamma \sim \mathcal{U}(0.5, 1.75)$. The gain is fixed at 1.

L. Brightness and Contrast Change (U05)

The brightness and contrast of the image are modified. The brightness change factor, contrast change factor are sampled from $\mathcal{U}(0.6, 1.4)$, $\mathcal{U}(0.6, 1.4)$, respectively. The image is then multiplied element-wise by its beam mask, to ensure black regions external to the beam remain black.

M. Depth Change Simulation (U06)

preserves the centre for linear beam shapes and preserves p_0 for convex beam shapes. The magnitude of the zoom transformation, d , is randomly sampled from a uniform distribution. Increasing the depth corresponds to zooming out ($d > 1$), while decreasing the depth corresponds to zooming in ($d < 1$).

N. Speckle Noise Simulation (U07)

Following Singh *et al.*'s method [28], this transformation calculates synthetic speckle noise and applies it to the ultrasound beam. Various parameters of the algorithm are randomly sampled upon each invocation. The lateral and axial resolutions for interpolation are random integers drawn from the ranges [35, 45] and [75, 85], respectively. The number of synthetic phasors is randomly drawn from the integer range [5, 10]. Sample points on the image are evenly spaced in Cartesian coordinates for linear beam shapes. For convex beams, the sample points are evenly spaced in polar coordinates.

O. Gaussian Noise Simulation (U08)

Multiplicative Gaussian noise is applied to the pixel intensities across the image. First, the standard deviation of the Gaussian noise, σ , is randomly drawn from the uniform distribution $\mathcal{U}(0.5, 2.5)$. Multiplicative Gaussian noise with mean 1 and standard deviation σ is then applied independently to each pixel in the image.

P. Salt and Pepper Noise Simulation (U09)

A random assortment of points in the image are set to 255 (salt) or 0 (pepper). The fractions of pixels set to salt and pepper values are sampled randomly according to $\mathcal{U}(0.001, 0.005)$.

Q. Horizontal Reflection (U10)

The image is reflected about the central vertical axis. This transformation is identical to U01.

TABLE XIV
MOBILENETV3SMALL BLOCK INDICES AND THE CORRESPONDING DIMENSIONS OF THE FEATURE MAPS THAT THEY OUTPUT, GIVEN AN INPUT OF SIZE $128 \times 128 \times 3$.

Block index	Feature map dimensions ($w \times h \times c$)
1	$32 \times 32 \times 16$
3	$16 \times 16 \times 24$
6	$8 \times 8 \times 40$
9	$4 \times 4 \times 96$
12	$4 \times 4 \times 576$

R. Rotation and Shift (U11)

A non-scaling affine transformation is applied to the image. More specifically, the image is translated and rotated. The horizontal component of the translation is sampled from $\mathcal{U}(-0.2, 0.2)$, as a fraction of the image's width. Similarly, the vertical component is sampled from $\mathcal{U}(-0.2, 0.2)$, as a fraction of the image's height. The rotation angle, in degrees, is sampled from $\mathcal{U}(-22.5, 22.5)$.

The Single Shot Detector (SSD) method [34] was employed to perform a cursory evaluation of the pretrained models on an object detection task. The PL task involved localizing instances of the pleural line in lung US images, which can be described as a bright horizontal line that is typically situated slightly below the vertical level of the ribs. It is only visible between the rib spaces, since bone blocks the ultrasound scan lines. The artifact represents the interface between the parietal and viscerai linings of the lung.

As in the classification experiments, we used the MobileNetV3Small architecture as the backbone of the network. The feature maps outputted from a designated set of layers were passed to the SSD regression and classification heads. We selected a range of layers whose feature maps had varying spatial resolution. Table XIV provides the identities and dimensions of the feature maps from the backbone that were fed to the SSD model heads. The set of default anchor box aspect ratios was manually specified after examining the distribution of bounding box aspect ratios in the training set. The 25th percentile was 2.894, and the 75th percentile was 4.989. The pleural line artifact typically has a much greater width than height. Accordingly, we designated the set of default anchor box aspect ratios (w/h) as {1, 2, 3, 4, 5}. Six anchor box scales were used. The first five were spaced out evenly over the range [0.023, 0.170], which correspond to the square roots of the minimum and maximum areas of the bounding box labels present in the training set, in normalized image coordinates. The final scale is 1, which is included by default.

The backbone and head were assigned initial learning rates of 0.002 and 0.02, respectively. Learning rates were annealed according to a cosine decay schedule. The model was trained for 30 epochs to minimize the loss function from the original SSD paper, which has a regression component for bounding box offsets and a classification component for distinguishing objects and background [34]. The weights corresponding to the epoch with the lowest validation loss were retained for test set evaluation.

As outlined in Section IV-A, statistical testing was per-

TABLE XV

FRIEDMAN TEST STATISTICS AND p -VALUES FOR MEAN CROSS-VALIDATION TEST AUC ATTAINED BY MODELS PRETRAINED USING AN ENTIRE DATA AUGMENTATION PIPELINE AND ABLATED VERSIONS OF IT.

Pipeline	AB		PE			
	F_r	Statistic	p -value	F_r	Statistic	
BYOL	30.73		0.000*	36.51		0.000*
AugUS-O	76.43		0.000*	18.91		0.091

* Statistically significant at $\alpha = 0.05$.

formed to detect differences between pretrained models trained using an ablated version of the BYOL and AugUS-O pipelines and baseline models pretrained on the original pipelines. Each ablated version of the pipeline was missing one transformation from the data augmentation pipeline. Ten-fold cross-validation conducted on the training set provided 10 samples of test AUC metrics for both the A-line versus B-line (AB) and pleural effusion (PE) binary classification tasks. The samples were taken as a proxy for test-time performance for linear classifiers trained on each of the above downstream tasks.

To determine whether the mean test AUC for each ablated model was different from the baseline model, hypothesis testing was conducted. The model pretrained using the original pipeline was the control group, while the models pretrained using ablated versions of the pipeline were the experimental groups. First, Friedman's test [35] was conducted to determine if there was any difference in the mean test AUC among the baseline and ablated models. We selected a nonparametric multiple comparisons test because of the lack of assumptions regarding normality or homogeneity of variances. Each collection had 10 samples. Table XV details the results of Friedman's test for each pipeline and classification task. Friedman's test detected differences among the collection of test AUC for both classification tasks with the BYOL pipeline. Only the AB task exhibited significant differences for the AugUS-O pipeline.

When the null hypothesis of the Friedman test was rejected, post-hoc tests were conducted to determine whether any of the test AUC means in the experimental groups were significantly different than the control group. The Wilcoxon Sign-Rank Test [36] was designated as the post-hoc test, due to its absence of any normality assumptions. Note that for each pipeline, n comparisons were performed, where n is the number of transformations within the pipeline. The Holm-Bonferroni correction [37] was applied to keep the family-wise error rate at $\alpha = 0.05$ for each pipeline/task combination. Results of the post-hoc tests are given in Table XVI. No post-hoc tests were performed for the AugUS-O pipeline evaluated on the PE task because the Friedman test revealed no significant differences.

Figs. 10, 11, and 12 provide several examples of positive pairs produced by the BYOL, AugUS-O, and AugUS-D pipelines, respectively. Each figure shows original images from LUSData, along with two views of each image that were produced by applying stochastic data augmentation twice to the original images.

For each of the AB and PE tasks, there were five experimental conditions: SimCLR pretraining with the BYOL

TABLE XVI

TEST STATISTICS (T) AND p -VALUES OBTAINED FROM THE WILCOXON SIGN-RANK POST-HOC TESTS THAT COMPARED LINEAR CLASSIFIERS TRAINED WITH ABLATED MODELS' FEATURES TO A CONTROL LINEAR CLASSIFIER TRAINED ON THE BASELINE MODEL. EXPERIMENTAL GROUPS ARE IDENTIFIED ACCORDING TO THE LEFT-OUT TRANSFORMATION, AS DEFINED IN TABLES II AND III.

Pipeline	Comparison	AB		PE	
		T	p -value	T	p -value
BYOL	$B00$	0	0.002*	0	0.002*
	$B01$	6	0.027	21	0.557
	$B02$	1	0.004*	3	0.010*
	$B03$	19	0.432	10	0.084
	$B04$	9	0.064	5	0.020
	$B05$	15	0.232	10	0.084
AugUS-O	$U00$	18	0.375	-	-
	$U01$	8	0.049	-	-
	$U02$	0	0.002*	-	-
	$U03$	0	0.002*	-	-
	$U04$	12	0.131	-	-
	$U05$	9	0.064	-	-
	$U06$	13	0.160	-	-
	$U07$	13	0.160	-	-
	$U08$	1	0.004*	-	-
	$U09$	1	0.004*	-	-
	$U10$	23	0.695	-	-
	$U11$	0	0.002*	-	-

* Statistically significant at family-wise error rate of 0.05.

pipeline, SimCLR pretraining with the AugUS-O pipeline, SimCLR pretraining with the AugUS-D pipeline, ImageNet weight initializations, and random weight initialization. The population consisted of 20 subsets of the training set that were split randomly by patient. The same splits were used across all conditions, reflecting a repeated measures design. The experiment was repeated separately for the AB and the PE task.

The Friedman Test Statistic (F_r) was 75.44 for AB, with a p -value of 0. For PE, the $F_r = 45.44$, and the p -value was 0. As such, the null hypothesis was rejected for both cases, indicating the existence of differences among the mean test AUC across conditions. The Wilcoxon Sign-Rank test was performed as a post-hoc test between each pair of populations. Tables XVII and XVIII provide all Wilcoxon Test Statistics, along with p -values and differences of the medians between conditions. The Bonferroni correction was applied to the p -values to keep the family-wise error rate to $\alpha = 0.05$. Statistically significant comparisons are indicated.

The C&R transform encourages pretrained representations to be invariant to scale. It is also believed that the C&R transform instills invariance between global and local views or between disjoint views of the same object type [30]. While the minimum area of the crop determines the magnitude of the scaling transformations, the aspect ratio range dictates the difference in distortion in both axes of the image. The default aspect ratio range is $[0.75, 1.33]$. We pretrained with the AugUS-D pipeline using a fixed aspect range of 1 and $c = 0.08$, which resulted in test AUC of 0.971 for AB and 0.881 for PE. Compared to the regular AugUS-D that uses the default aspect ratio range (Table 5), AB test AUC is unchanged; however, PE test AUC decreased by 0.016.

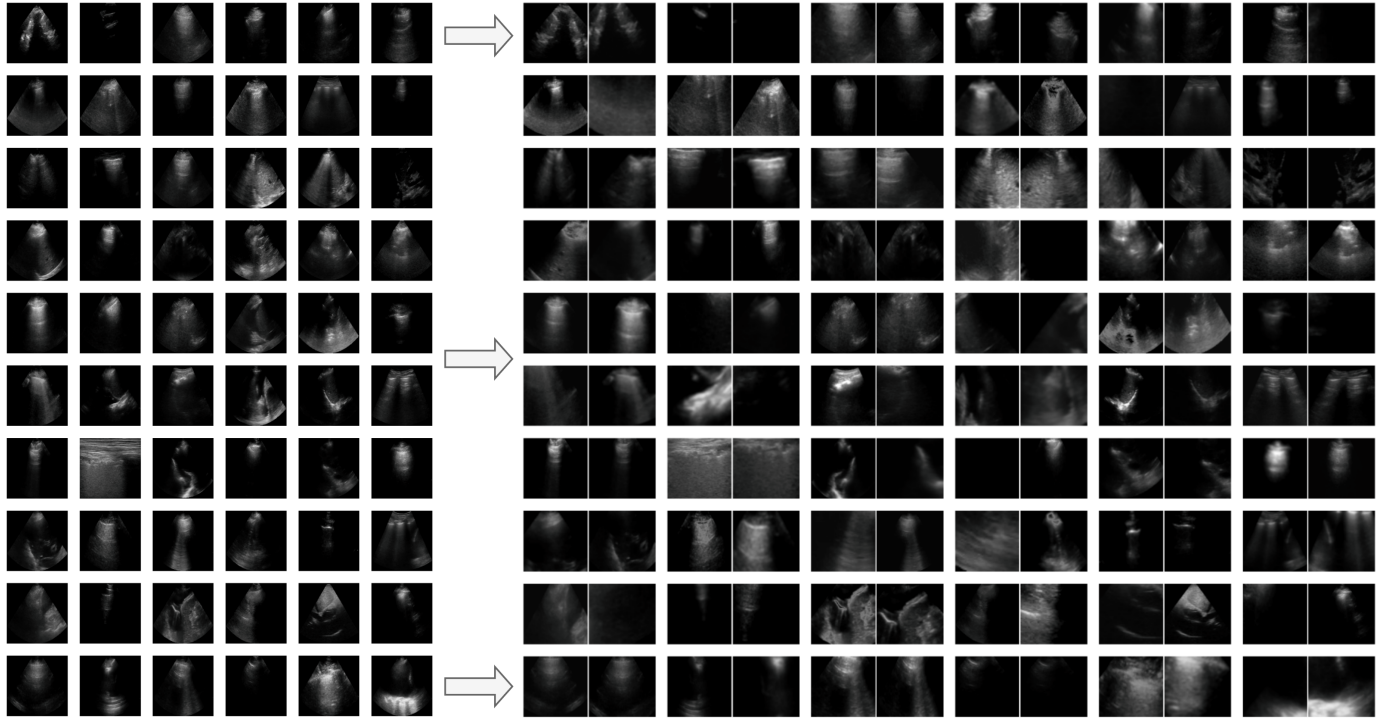


Fig. 10. Examples of lung ultrasound images (left) and positive pairs produced using the BYOL pipeline (right).

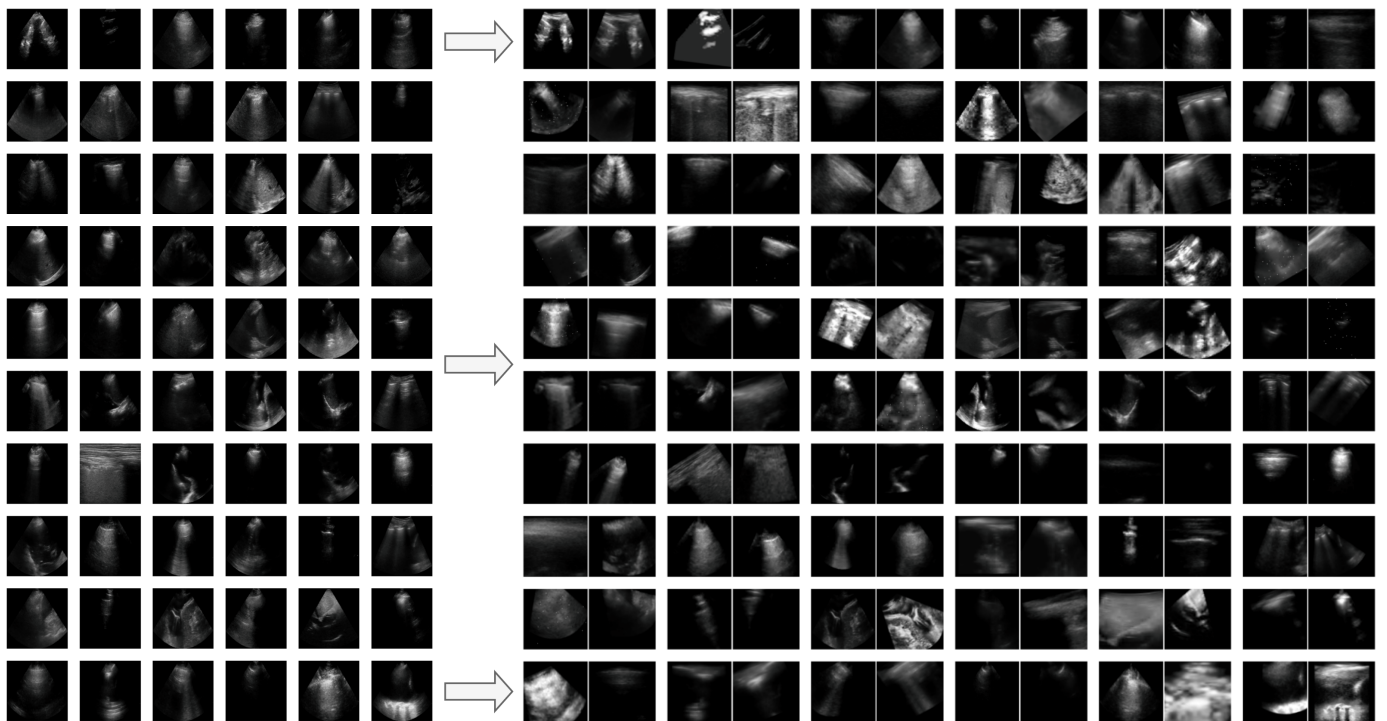


Fig. 11. Examples of lung ultrasound images (left) and positive pairs produced using the AugUS-O pipeline (right).

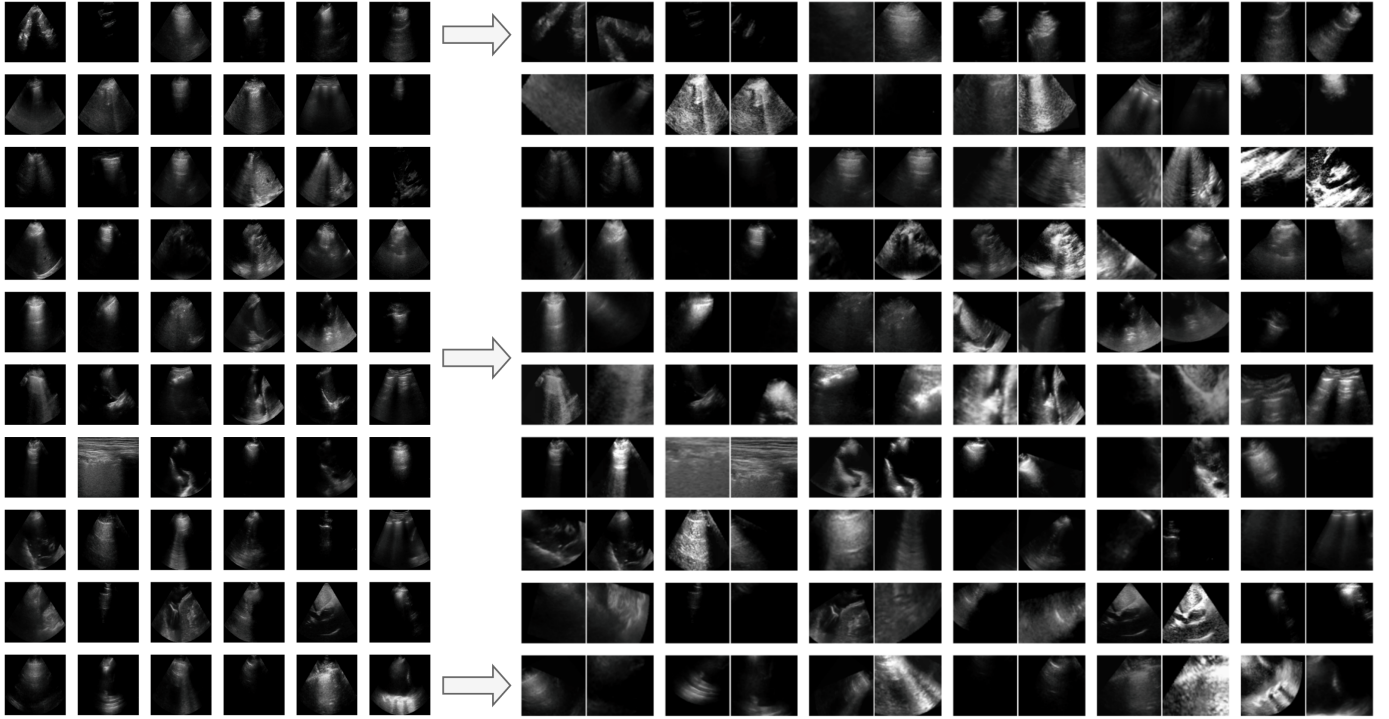


Fig. 12. Examples of lung ultrasound images (left) and positive pairs produced using the AugUS-D pipeline (right).

TABLE XVII

TEST STATISTICS (T) AND p -VALUES OBTAINED FROM THE WILCOXON SIGN-RANK POST-HOC TESTS COMPARING LUSDATA TEST AUC ON AB FOR CLASSIFIERS TRAINED ON SUBSETS OF THE TRAINING SET. FOR COMPARISON a/b , $\Delta := \text{MEDIAN}(b) - \text{MEDIAN}(a)$. THE DISPLAYED p -VALUES HAVE BEEN ADJUSTED ACCORDING TO THE BONFERRONI CORRECTION TO CONTROL THE FAMILY-WISE ERROR RATE.

Comparison	T	p -value	Δ
Random / ImageNet	3	$9.4 \times 10^{-5}^*$	-0.058
Random / BYOL	0	$1.9 \times 10^{-5}^*$	0.044
Random / AugUS-O	12	$1.3 \times 10^{-3}^*$	0.019
Random / AugUS-D	0	$1.9 \times 10^{-5}^*$	0.042
ImageNet / BYOL	0	$1.9 \times 10^{-5}^*$	0.100
ImageNet / AugUS-O	0	$1.9 \times 10^{-5}^*$	0.078
ImageNet / AugUS-D	0	$1.9 \times 10^{-5}^*$	0.100
BYOL / AugUS-O	0	$1.9 \times 10^{-5}^*$	-0.024
BYOL / AugUS-D	61	1.0	-0.002
AugUS-O / AugUS-D	0	$1.9 \times 10^{-5}^*$	0.022

* Statistically significant at family-wise error rate of 0.05.

Lastly, we conducted pretraining on LUSData using only the C&R transformation; that is, the data augmentation pipeline was [B00]. Recent work by Moutakanni *et al.* [41] suggests that, with sufficient quantities of training data, competitive performance in downstream computer vision tasks can be achieved using crop and resize as the sole transformation in joint embedding SSL. Linear evaluation of a feature extractor pretrained with only C&R yielded test AUC of 0.964 and 0.874 on AB and PE, respectively. Compared to the linear evaluations presented in Section 4, these metrics are greater than those achieved using AugUS-O, but less than those achieved with BYOL or AugUS-D. It is evident that C&R is a powerful transformation for detecting local objects.

TABLE XVIII

TEST STATISTICS (T) AND p -VALUES OBTAINED FROM THE WILCOXON SIGN-RANK POST-HOC TESTS COMPARING LUSDATA TEST AUC ON PE FOR CLASSIFIERS TRAINED ON SUBSETS OF THE TRAINING SET. FOR COMPARISON a/b , $\Delta := \text{MEDIAN}(b) - \text{MEDIAN}(a)$. THE DISPLAYED p -VALUES HAVE BEEN ADJUSTED ACCORDING TO THE BONFERRONI CORRECTION TO CONTROL THE FAMILY-WISE ERROR RATE.

Comparison	T	p -value	Δ
Random / ImageNet	1	$3.8 \times 10^{-5}^*$	-0.127
Random / BYOL	31	$4.2 \times 10^{-2}^*$	0.025
Random / AugUS-O	16	$3.2 \times 10^{-3}^*$	0.030
Random / AugUS-D	5	$1.9 \times 10^{-4}^*$	0.036
ImageNet / BYOL	1	$3.8 \times 10^{-5}^*$	0.152
ImageNet / AugUS-O	0	$1.9 \times 10^{-5}^*$	0.157
ImageNet / AugUS-D	1	$3.8 \times 10^{-5}^*$	0.163
BYOL / AugUS-O	57	7.6×10^{-1}	0.005
BYOL / AugUS-D	53	5.3×10^{-1}	0.011
AugUS-O / AugUS-D	78	1	0.006

* Statistically significant at family-wise error rate of 0.05.

REFERENCES

- [1] Y. Wang, X. Ge, H. Ma, S. Qi, G. Zhang, and Y. Yao, “Deep learning in medical ultrasound image analysis: a review,” *IEEE Access*, vol. 9, pp. 54310–54324, 2021.
- [2] Q. Yang, J. Wei, X. Hao, D. Kong, X. Yu, T. Jiang, J. Xi, W. Cai, Y. Luo, X. Jing, *et al.*, “Improving B-mode ultrasound diagnostic performance for focal liver lesions using deep learning: A multicentre study,” *EBioMedicine*, vol. 56, 2020.
- [3] A. Ghorbani, D. Ouyang, A. Abid, B. He, J. H. Chen, R. A. Harrington, D. H. Liang, E. A. Ashley, and J. Y. Zou, “Deep learning interpretation of echocardiograms,” *NPJ digital medicine*, vol. 3, no. 1, p. 10, 2020.
- [4] B. VanBerlo, D. Wu, B. Li, M. A. Rahman, G. Hogg, B. VanBerlo, J. Tschirhart, A. Ford, J. Ho, J. McCauley, *et al.*, “Accurate assessment of the lung sliding artefact on lung ultrasonography using a deep learning approach,” *Computers in biology and medicine*, vol. 148, p. 105953, 2022.

- [5] S. Liu, Y. Wang, X. Yang, B. Lei, L. Liu, S. X. Li, D. Ni, and T. Wang, “Deep learning in medical ultrasound analysis: a review,” *Engineering*, vol. 5, no. 2, pp. 261–275, 2019.
- [6] M. Y. Ansari, I. A. C. Mangalote, P. K. Meher, O. Aboumarzouk, A. Al-Ansari, O. Halabi, and S. P. Dakua, “Advancements in deep learning for B-mode ultrasound segmentation: A comprehensive review,” *IEEE Transactions on Emerging Topics in Computational Intelligence*, 2024.
- [7] B. VanBerlo, J. Hoey, and A. Wong, “A survey of the impact of self-supervised pretraining for diagnostic tasks in medical X-ray, CT, MRI, and ultrasound,” *BMC Medical Imaging*, vol. 24, no. 1, p. 79, 2024.
- [8] R. Balestrieri and Y. LeCun, “Contrastive and non-contrastive self-supervised learning recover global and local spectral embedding methods,” in *Advances in Neural Information Processing Systems* (S. Koyejo, S. Mohamed, A. Agarwal, D. Belgrave, K. Cho, and A. Oh, eds.), vol. 35, pp. 26671–26685, Curran Associates, Inc., 2022.
- [9] S. Azizi, B. Mustafa, F. Ryan, Z. Beaver, J. Freyberg, J. Deaton, A. Loh, A. Karthikesalingam, S. Kornblith, T. Chen, et al., “Big self-supervised models advance medical image classification,” in *Proceedings of the IEEE/CVF international conference on computer vision*, pp. 3478–3488, 2021.
- [10] Q. Zhao, Z. Liu, E. Adeli, and K. M. Pohl, “Longitudinal self-supervised learning,” *Medical image analysis*, vol. 71, p. 102051, 2021.
- [11] S. Basu, S. Singla, M. Gupta, P. Rana, P. Gupta, and C. Arora, “Unsupervised contrastive learning of image representations from ultrasound videos with hard negative mining,” in *International Conference on Medical Image Computing and Computer-Assisted Intervention*, pp. 423–433, Springer, 2022.
- [12] V. Cabannes, B. Kiani, R. Balestrieri, Y. LeCun, and A. Bietti, “The SSL interplay: Augmentations, inductive bias, and generalization,” in *International Conference on Machine Learning*, pp. 3252–3298, PMLR, 2023.
- [13] J.-B. Grill, F. Strub, F. Altché, C. Tallec, P. Richemond, E. Buchatskaya, C. Doersch, B. Avila Pires, Z. Guo, M. Gheshlaghi Azar, et al., “Bootstrap your own latent-a new approach to self-supervised learning,” *Advances in neural information processing systems*, vol. 33, pp. 21271–21284, 2020.
- [14] A. Fernandez-Quilez, T. Eftestøl, S. R. Kjosavik, M. Goodwin, and K. Oppedal, “Contrasting axial T2W mri for prostate cancer triage: A self-supervised learning approach,” in *2022 IEEE 19th International Symposium on Biomedical Imaging (ISBI)*, pp. 1–5, IEEE, 2022.
- [15] D. Anand, P. Annangi, and P. Sudhakar, “Benchmarking self-supervised representation learning from a million cardiac ultrasound images,” in *Proceedings of the Annual International Conference of the IEEE Engineering in Medicine and Biology Society, EMBS*, vol. 2022-July, pp. 529–532, Institute of Electrical and Electronics Engineers Inc., 2022. ISSN: 1557170X.
- [16] M. Saeed, R. Muhtaseb, and M. Yaqub, “Contrastive pretraining for echocardiography segmentation with limited data,” *Lecture Notes in Computer Science (including subseries Lecture Notes in Artificial Intelligence and Lecture Notes in Bioinformatics)*, vol. 13413 LNCS, pp. 680–691, 2022. ISBN: 9783031120527 Publisher: Springer Science and Business Media Deutschland GmbH.
- [17] N.-Q. Nguyen and T.-S. Le, “A semi-supervised learning method to remedy the lack of labeled data,” in *2021 15th International Conference on Advanced Computing and Applications (ACOMP)*, pp. 78–84, IEEE, 2021.
- [18] Y. Chen, C. Zhang, L. Liu, C. Feng, C. Dong, Y. Luo, and X. Wan, “USCL: Pretraining deep ultrasound image diagnosis model through video contrastive representation learning,” in *Medical Image Computing and Computer Assisted Intervention—MICCAI 2021: 24th International Conference, Strasbourg, France, September 27–October 1, 2021, Proceedings, Part VIII 24*, pp. 627–637, Springer, 2021.
- [19] Y. Chen, C. Zhang, C. H. Ding, and L. Liu, “Generating and weighting semantically consistent sample pairs for ultrasound contrastive learning,” *IEEE Transactions on Medical Imaging*, 2022.
- [20] C. Zhang, Y. Chen, L. Liu, Q. Liu, and X. Zhou, “HiCo: Hierarchical contrastive learning for ultrasound video model pretraining,” in *Proceedings of the Asian Conference on Computer Vision*, pp. 229–246, 2022.
- [21] B. VanBerlo, A. Wong, J. Hoey, and R. Arntfield, “Intra-video positive pairs in self-supervised learning for ultrasound,” *Frontiers in Imaging*, vol. 3, 2024.
- [22] L. Chen, J. Rubin, J. Ouyang, N. Balaraju, S. Patil, C. Mehanian, S. Kulhare, R. Millin, K. W. Gregory, C. R. Gregory, et al., “Contrastive self-supervised learning for spatio-temporal analysis of lung ultrasound videos,” in *2023 IEEE 20th International Symposium on Biomedical Imaging (ISBI)*, pp. 1–5, IEEE, 2023.
- [23] A. Ebadi, P. Xi, A. MacLean, A. Florea, S. Tremblay, S. Kohli, and A. Wong, “COVIDx-US: An open-access benchmark dataset of ultrasound imaging data for AI-driven COVID-19 analytics,” *Front. Biosci. (Landmark Ed.)*, vol. 27, p. 198, June 2022.
- [24] E. Z. Zeng, A. Ebadi, A. Florea, and A. Wong, “COVID-Net L2C-ULTRA: An explainable linear-convex ultrasound augmentation learning framework to improve COVID-19 assessment and monitoring,” *Sensors*, vol. 24, no. 5, p. 1664, 2024.
- [25] L. Birgé and P. Massart, *From model selection to adaptive estimation*. Springer, 1997.
- [26] S. M. Pizer, E. P. Amburn, J. D. Austin, R. Cromartie, A. Geselowitz, T. Greer, B. ter Haar Romeny, J. B. Zimmerman, and K. Zuiderweld, “Adaptive histogram equalization and its variations,” *Computer vision, graphics, and image processing*, vol. 39, no. 3, pp. 355–368, 1987.
- [27] D. Vilimek, J. Kubicek, M. Golian, R. Jaros, R. Kahankova, P. Hanzlikova, D. Barvik, A. Krestanova, M. Penhaker, M. Cerny, et al., “Comparative analysis of wavelet transform filtering systems for noise reduction in ultrasound images,” *Plos one*, vol. 17, no. 7, p. e0270745, 2022.
- [28] P. Singh, R. Mukundan, and R. de Ryke, “Synthetic models of ultrasound image formation for speckle noise simulation and analysis,” in *2017 International Conference on Signals and Systems (ICSigSys)*, pp. 278–284, IEEE, 2017.
- [29] A. Howard, M. Sandler, G. Chu, L.-C. Chen, B. Chen, M. Tan, W. Wang, Y. Zhu, R. Pang, V. Vasudevan, et al., “Searching for MobileNetV3,” in *Proceedings of the IEEE/CVF international conference on computer vision*, pp. 1314–1324, 2019.
- [30] T. Chen, S. Kornblith, M. Norouzi, and G. Hinton, “A simple framework for contrastive learning of visual representations,” in *International conference on machine learning*, pp. 1597–1607, PMLR, 2020.
- [31] B. VanBerlo, B. Li, J. Hoey, and A. Wong, “Self-supervised pretraining improves performance and inference efficiency in multiple lung ultrasound interpretation tasks,” *IEEE Access*, vol. 11, pp. 135696–135707, 2023.
- [32] J. Deng, W. Dong, R. Socher, L.-J. Li, K. Li, and L. Fei-Fei, “ImageNet: A large-scale hierarchical image database,” in *2009 IEEE conference on computer vision and pattern recognition*, pp. 248–255, Ieee, 2009.
- [33] Y. You, J. Li, S. Reddi, J. Hseu, S. Kumar, S. Bhojanapalli, X. Song, J. Demmel, K. Keutzer, and C.-J. Hsieh, “Large batch optimization for deep learning: Training bert in 76 minutes,” *arXiv preprint arXiv:1904.00962*, 2019.
- [34] W. Liu, D. Anguelov, D. Erhan, C. Szegedy, S. Reed, C.-Y. Fu, and A. C. Berg, “SSD: Single shot multibox detector,” in *Computer Vision-ECCV 2016: 14th European Conference, Amsterdam, The Netherlands, October 11–14, 2016, Proceedings, Part I 14*, pp. 21–37, Springer, 2016.
- [35] M. Friedman, “A comparison of alternative tests of significance for the problem of m rankings,” *The annals of mathematical statistics*, vol. 11, no. 1, pp. 86–92, 1940.
- [36] F. Wilcoxon, “Individual comparisons by ranking methods,” *Biometrics Bulletin*, vol. 1, no. 6, pp. 80–83, 1945.
- [37] S. Holm, “A simple sequentially rejective multiple test procedure,” *Scandinavian journal of statistics*, pp. 65–70, 1979.
- [38] I. Blazic, C. Cogliati, N. Flor, G. Frijia, M. Kawooya, M. Umbrello, S. Ali, M.-L. Baranne, Y.-J. Cho, R. Pitcher, et al., “The use of lung ultrasound in COVID-19,” *ERJ Open Research*, vol. 9, no. 1, 2023.
- [39] A. Bardes, J. Ponce, and Y. LeCun, “VICReg: Variance-Invariance-Covariance Regularization for Self-Supervised Learning,” in *International Conference on Learning Representations*, 2022.
- [40] K. Kim, F. Macruz, D. Wu, C. Bridge, S. McKinney, A. A. Al Saud, E. Sharaf, A. Pely, P. Danset, T. Duffy, et al., “Point-of-care ai-assisted stepwise ultrasound pneumothorax diagnosis,” *Physics in Medicine & Biology*, vol. 68, no. 20, p. 205013, 2023.
- [41] T. Moutakanni, M. Oquab, M. Szafraniec, M. Vakalopoulou, and P. Bojanowski, “You don’t need domain-specific data augmentations when scaling self-supervised learning,” in *The Thirty-eighth Annual Conference on Neural Information Processing Systems*, 2024.